

Key Points:

- Hierarchical clustering of longitudinal river profiles allows identification of landscape similarity
- Analyzing spatial patterns of similar river profiles allows linking to a common set of lithological, climatic, or tectonic drivers
- Clustering detects landscape heterogeneity that is not identified by normalized channel steepness analysis

Supporting Information:

- Supporting Information S1
- Video S1
- Video S2
- Data Set S1
- Data Set S2

Correspondence to:

F. J. Clubb,
clubb@uni-potsdam.de

Citation:

Clubb, F. J., Bookhagen, B., & Rheinwalt, A. (2019). Clustering river profiles to classify geomorphic domains. *Journal of Geophysical Research: Earth Surface*, 124. <https://doi.org/10.1029/2019JF005025>

Received 5 FEB 2019

Accepted 25 APR 2019

Accepted article online 1 MAY 2019

Clustering River Profiles to Classify Geomorphic Domains

Fiona J. Clubb¹, Bodo Bookhagen¹, and Aljoscha Rheinwalt¹

¹Institute of Geosciences, University of Potsdam, Potsdam, Germany

Abstract The structure and organization of river networks has been used for decades to investigate the influence of climate and tectonics on landscapes. The majority of these studies either analyze rivers in profile view by extracting channel steepness or calculate planform metrics such as drainage density. However, these techniques rely on the assumption of homogeneity: that intrinsic and external factors are spatially or temporally invariant over the measured profile. This assumption is violated for the majority of Earth's landscapes, where variations in uplift rate, rock strength, climate, and geomorphic process are almost ubiquitous. We propose a method for classifying river profiles to identify landscape regions with similar characteristics by adapting hierarchical clustering algorithms developed for time series data. We first test our clustering on two landscape evolution scenarios and find that we can successfully cluster regions with different erodibility and detect the transient response to sudden base level fall. We then test our method in two real landscapes: first in Bitterroot National Forest, Idaho, where we demonstrate that our method can detect transient incision waves and the topographic signature of fluvial and debris flow process regimes; and second, on Santa Cruz Island, California, where our technique identifies spatial patterns in lithology not detectable through normalized channel steepness analysis. By calculating channel steepness separately for each cluster, our method allows the extraction of more reliable steepness metrics than if calculated for the landscape as a whole. These examples demonstrate the method's ability to disentangle fluvial morphology in complex lithological and tectonic settings.

1. Introduction

For many decades, the study of river networks has been a core concept in geomorphic theory and research. Both the planforms and profiles of fluvial channels have been used to answer diverse problems, such as constraining changes in uplift rates (e.g., Kirby et al., 2003; Kirby & Whipple, 2001; Lavé & Avouac, 2001; Nennewitz et al., 2018), deducing throw rates from faulting (e.g., Whittaker et al., 2008), isolating patterns of drainage capture (e.g., Giachetta & Willett, 2018; Willett et al., 2014), detecting signatures of climate (e.g., Hobley et al., 2012; Roe et al., 2002; Ranjbar et al., 2018; Seybold et al., 2017), and quantifying the impact of different erosional processes on drainage networks (e.g., Bookhagen & Strecker, 2012; Clubb et al., 2016; DiBiase et al., 2010; Hooshyar et al., 2017; Neely et al., 2017; Olen et al., 2016; Stock & Dietrich, 2003).

The majority of studies that use the morphology of longitudinal river profiles most commonly derive a metric representing channel gradient, S . The earliest work on river long profiles by Gilbert (1877) deduced qualitatively that, when uplift is equal to erosion, plotting elevation against distance upstream along a river profile should result in a concave-up curve. This relationship means that the headwaters of a channel will inevitably have a steeper gradient than subsequent reaches downstream. Following on from this, channel gradient has been shown through many empirical studies to decrease as a function of drainage area, A (Flint, 1974; Morisawa, 1962; Tarboton et al., 1989). This empirical relationship is commonly referred to as Flint's law:

$$S = k_s A^{-\theta}, \quad (1)$$

where θ is referred to as the concavity index and k_s as the steepness index. If we plot S and A at every point along a channel profile on a logarithmic scale, we can perform a least squares fit of the power law in equation (1) to estimate k_s and θ . The exponent of the fit represents the concavity index, which dictates how rapidly the gradient of the channel will decline with increasing area. The amplitude of the fit represents the steepness index, which is determined by the gradient of the channel. As k_s and θ are strongly correlated when determined from this fitting, k_s is commonly normalized by a reference concavity index (θ_{ref}) and referred to as k_{sn} . Wobus et al. (2006) suggest that θ_{ref} should be selected as the mean θ of channel segments determined to be in steady state, although recent work has shown that θ can vary significantly over small

spatial scales, meaning that this is in practice challenging to determine (Mudd et al., 2018). Normalized channel steepness can be calculated for each point along a channel network as

$$k_{sn,i} = A_i^{\theta_{ref}} S_i, \quad (2)$$

where the subscript i refers to a data point. This normalized channel steepness is often used in tectonic geomorphology to infer variations in uplift rate across different catchments or orogens (e.g., Kirby & Whipple, 2001; 2012; Snyder et al., 2000; Wobus et al., 2006). Recently, additional techniques have been developed to extract channel steepness by plotting an upstream integral of drainage area, referred to as χ , against elevation along the channel, to try and avoid common problems with noise inherent in deriving slope data from digital elevation models (DEMs; e.g., Harkins et al., 2007; Hergarten et al., 2016; Mudd et al., 2014, 2018; Perron & Royden, 2013; Whipple et al., 2017).

The planform geometry of river networks has also been used to deduce information about the driving factors controlling landscape morphology. In a seminal paper, Horton (1945) defined the fundamental network property of drainage density (D_d), which quantifies landscape dissection. Many authors have attempted to link drainage density to external factors such as landscape erosion rate (Clubb et al., 2016), precipitation (Abrahams, 1984; Melton, 1957; Sangireddy et al., 2016), vegetation cover (Collins & Bras, 2010; Istanbulluoglu & Bras, 2005), and lithology (Oguchi, 1997). Others have focused on analyzing the angle between tributary junctions (e.g., Horton, 1945; Howard, 1971a, 1971b; Hooshyar et al., 2017; Seybold et al., 2017). Distinct populations of junction angles have been found from the analysis of millions of tributary junctions, which have been linked to both climate (Seybold et al., 2017) and the relative importance of colluvial and fluvial incision processes (Hooshyar et al., 2017).

These properties of fluvial networks, both in profile and plan view, compose a set of diagnostic tools for examining fluvial response to external forcing, such as climate, tectonics, or base level change, as well as the influence of internal processes such as lithology or geomorphic processes. However, extracting these metrics generally requires some assumption of spatial homogeneity. For example, when extracting channel steepness estimates, if the data are taken together from the catchment as a whole, we must assume that the landscape is in “steady state”: that the uplift rate U is balanced by the fluvial incision rate, E . In the majority of Earth’s landscapes, this assumption breaks down, especially in mountainous regions where geomorphic research tends to be focused. Horizontal and vertical plate motions frequently lead to landscape readjustment, propagating transient signals through river networks in the form of steepened channel reaches or knickpoints (e.g., Kirby & Whipple, 2012). Over the Quaternary, variations in climate have led to the frequent advance and retreat of ice sheets, which raise and lower sea level, resulting in the transmission of base level change signals into the fluvial system (e.g., Anthony & Granger, 2007; Gran et al., 2013). Alongside these temporal forcings, spatial heterogeneity is almost ubiquitous within upland landscapes: uplift rates may vary both along and with distance away from fault zones (e.g., Peacock & Sanderson, 1991), leading to morphological adjustment in channel profiles (Roda-Boluda & Whittaker, 2016; Whittaker et al., 2008). Changes in rock strength across lithological boundaries have shown to fundamentally affect the steepness of river channels (e.g., Duvall et al., 2004), while density changes can result in spatial variations in uplift rates through isostatic rebound (Braun et al., 2014). Integrating these effects means that virtually no landscape on Earth truly meets the criteria for steady state.

Along with these difficulties caused by spatial and temporal landscape heterogeneity, we also face new challenges caused by the exponential increase in the availability of topographic data in recent decades. We can now capture the Earth’s surface at unprecedented spatial resolutions, which, although generally beneficial, can result in increasing noise due to local effects such as vegetation, bedrock outcrops, or anthropogenic features. This noise can obscure potential signals, and often means that significant smoothing must be performed on the data before any analysis can take place (e.g., Aiken & Brierley, 2013; Schwanghart & Scherler, 2017). Furthermore, the collection of high-resolution data over large spatial scales means that data sets are often computationally intensive to analyze. Traditional techniques for analyzing river networks often struggle to deal with the sheer volume of data that is now available. Therefore, there is a real need to develop new methods of analyzing topographic data that can best extract potential signals from data sets with both large computational sizes and higher noise levels.

In this contribution we suggest a potential solution for tackling the problem of analyzing river networks in heterogeneous landscapes, by developing techniques for separating river profiles into groups with similar

morphologies prior to the extraction of network geometry. We draw inspiration from the well-developed field of time series analysis and adapt one-dimensional time series clustering algorithms for use with geomorphic data. These algorithms are often used in an exploratory sense on large data sets, in order to reduce the volume of data and distinguish between signal and noise, making them ideal for use with high-resolution topography data sets. We suggest that these techniques can be used in geomorphic research to differentiate parts of the fluvial network with different tectonic, climatic, or lithological histories. First, we detail our methodology for adapting these clustering techniques for use with geomorphic data and then test our method using simple numerical modeling scenarios. This allows us to demonstrate the ability of the method to correctly identify similar regions within synthetic landscapes where the uplift and erosion histories are constrained. We then provide two example applications from Bitterroot National Forest, Idaho, and from Santa Cruz Island, California, to demonstrate the potential that these techniques hold for disentangling fluvial morphology in complex lithological and tectonic settings.

2. Clustering of One-Dimensional Data

Any analysis of river profiles from gridded digital elevation data involves taking a two-dimensional representation of the land surface and reducing it to one dimension: we start with a DEM, or a regular array of elevation values, and we reduce this to a series of either elevations (z) or channel gradients ($\partial z / \partial x$), which vary with some distance, x . Our goal is therefore to take a series of lines, where each line is the elevation or gradient profile of one river, and identify groupings which have similar characteristics. This grouping in one dimension allows us to compare the morphology of river profiles separately from their spatial location.

Clustering algorithms have been used to group one-dimensional data in many diverse fields, including economics (e.g., Abido, 2003), computational science (e.g., March, 1983), biological science (e.g., Eisen et al., 1998; Girvan & Newman, 2002), and environmental science (e.g., Maschler et al., 2018; Rheinwalt et al., 2015; Smith et al., 2017). Many applications of one-dimensional clustering algorithms deal with the analysis of time series data, for example, where a metric such as air temperature is measured at the same time intervals at a series of different spatial locations. The goal of the algorithms is to identify which profiles show a similar change in the chosen metric through time (Aghabozorgi et al., 2015). This problem is analogous to that of river profile analysis, except we wish to analyze channel gradient as the chosen metric, and we look at differences downstream along each profile rather than through time.

Classification via clustering techniques has a number of key advantages. Firstly, these algorithms are unsupervised: groups are created purely based on how similar objects are within a group, rather than using any predefined classification labels (Jain et al., 1999; Jain, 2010). In terms of geomorphological research, this is an advantage, as it means we do not need to make any a priori assumptions about the impact of external forcing such as the influence of climate, tectonics, or lithology, which are often difficult to constrain on a landscape scale. Furthermore, if one has a large number of data points, or measurement locations, clustering allows a reduction in data volume and can aid in distinguishing signal from noise (Aghabozorgi et al., 2015). Here we specifically employ agglomerative hierarchical clustering for the classification of river profiles. These algorithms work on the basis that each data point starts in its own cluster, which are then iteratively merged until only one cluster remains. This merging is done based on a similarity (or dissimilarity) metric, which describes how similar each profile is to every other one, where the most similar profiles are merged first. A key advantage of this technique is that we preserve information on how each cluster is related to the others, or a hierarchy, which is often shown in the form of a *dendrogram*. Dendograms can provide useful information on the appropriate number of clusters in a data set (e.g., Murtagh & Contreras, 2012).

3. Methodology

Here we set out our methodology for applying agglomerative hierarchical clustering algorithms to river profile analysis. We cluster the profiles based on the pattern of channel gradient as a function of distance downstream from the channel head, with the aim of distinguishing profiles with similar climatic, tectonic, or lithological forcing.

3.1. Selection of River Profiles

First, we identify a starting point of each river profile using a curvature-based approach to identifying channel heads following Pelletier (2013), Clubb et al. (2014), and Grieve et al. (2016). This algorithm has been

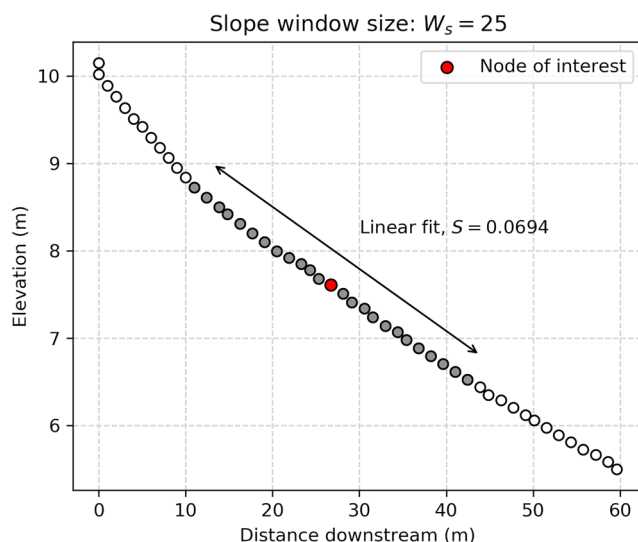


Figure 1. Method for calculating gradient along the channel profile, where the example channel nodes are shown as open circles with the node of interest highlighted in red. At each point, n nodes are selected upstream and downstream of the node of interest, where $n = (W_s - 1)/2$. The example here shows $W_s = 25$, meaning that 12 additional nodes are selected on either side of the node. In this case a linear fit through those 25 nodes would result in a gradient of 0.0694.

shown to perform well on high-resolution topographic data (Grieve et al., 2016), but we provide alternative methods, such as drainage area thresholds, within the clustering algorithm. From every channel head, we route flow using a steepest descent algorithm (O'Callaghan & Mark, 1984) to the outlet. Every pixel in the profile, which we refer to hereafter as channel node, is assigned an elevation (m), distance from the channel head (m), and drainage area (m^2). We calculate the channel gradient at each node using a moving window of a defined size W_s , which we keep constant at 25 nodes for 1 m resolution topographic data. This should be adjusted based on the DEM resolution (see section 6). For $W_s = 25$, we fit a line through 12 nodes upstream and downstream of the node of interest, plus the node itself, and define the gradient of the node of interest as the slope of the line (Figure 1). For the first and last 12 nodes of the profile, we calculate the slope only over the radius that is available (e.g., for the first node, over the 12 nodes downslope from this point). Although this approach assumes a linear fit to the channel profile, this error is negligible at the window-sized scale. However, W_s should be adjusted based on the DEM resolution to avoid oversmoothing the channel profiles.

After extracting the profiles, we then separate the channel network by stream order following Strahler (1957). This allows us to ensure that we are comparing profiles with a similar discharge and drainage area. The user may select the stream order of interest (S_o) within our implementation of the algorithm. If a stream order greater than 1 is selected, the longest channel in each basin of that order will be extracted (e.g., if $S_o = 3$, then the longest channel in each third-order basin). Clustering over

higher stream orders will result in the extraction of relatively longer but fewer profiles compared to the selection of first-order channels. Although there may be some variation in discharge and drainage area between profiles of the same stream order, separating the network by drainage area leads to breaks in the profiles at tributary junctions as well as overlap of the profiles in the downstream direction, which must be avoided in order to perform the clustering successfully. We note here that other types of stream ordering, such as Shreve ordering (Shreve, 1966), could also be used to perform the clustering in future applications of the method.

Typically, the input data for clustering algorithms are regularly spaced, such as in time series analysis (e.g., where data may be daily or yearly). Therefore, we sample the gradient at a regular flow distance step along each profile, such that each profile can be compared to every other. However, as we calculate flow distance from the DEM using a steepest descent algorithm, the flow distance between pixels can vary depending on whether the flow is directed along one of the cardinal flow directions (in which case the flow distance D will be equal to the grid resolution, G_r), or whether it is directed along a diagonal ($D = \sqrt{2}G_r$). Therefore, in order to compare and cluster different profiles, we must first reassign the flow distances along each profile so that they are regularly spaced. To do this, we assign the channel head in each profile a distance of 0, and then create an array of flow distances with an even spacing to the end of the profile. The distance spacing can be determined by the user, but in our implementation must be greater than $\sqrt{2}G_r$. After this array is created, we iterate through each element in this array, find the nearest flow distance to it from the original profile, and assign the node its new flow distance from the regularly spaced array. This means that no interpolation of the flow distance data is required. We recommend that this distance spacing should be the minimum integer distance above $\sqrt{2}G_r$: for 1-m resolution data, for example, the minimum spacing would be 2 m. After assigning the profiles to a regularly spaced array, we then remove profiles which are shorter than a defined threshold length, or L_T . This is to ensure that there are enough nodes in each profile to perform a meaningful clustering. This selection of profiles therefore requires four user-defined parameters in total: details and recommendations for these parameters are set out in Table 1.

3.2. Clustering

Following the extraction of the river profiles, we then use clustering techniques to perform a classification. The first step to perform the clustering analysis is to determine how similar each profile is to every other one. Many different approaches have been taken in time series clustering analysis to determine a metric describing the similarity, or dissimilarity, between time series, such as Euclidean-based metrics,

Table 1
Notation and Details of User-Defined Parameters Required by the Method

Parameter	Details	Suggested value
W_s	Window size for calculation of channel slope	25 nodes
S_T	Regular step spacing along profiles	$S_T > \sqrt{2G_r}$ ^a
L_T	Minimum length of each profile	Five nodes
S_o	Stream order of profiles	1

Note. The suggested values have been tested on 1-m resolution topographic data.

^a G_r : spatial resolution of the digital elevation model.

Pearson correlations, dynamic time warping, or probability-based distances (e.g., Liao, 2005). Here we calculate a Euclidean-based dissimilarity measure (d_R) between each pair of profiles in channel gradient space (Figure 2a). If we let X and Y each represent an array of length n of channel gradients, then the dissimilarity (d) between them can be computed by

$$d = \sqrt{\sum_{i=1}^n (X_i - Y_i)^2}, \quad (3)$$

where i represents an element in the array. We then divide d by n , the number of points in the profile, to obtain d_R :

$$d_R = d/n. \quad (4)$$

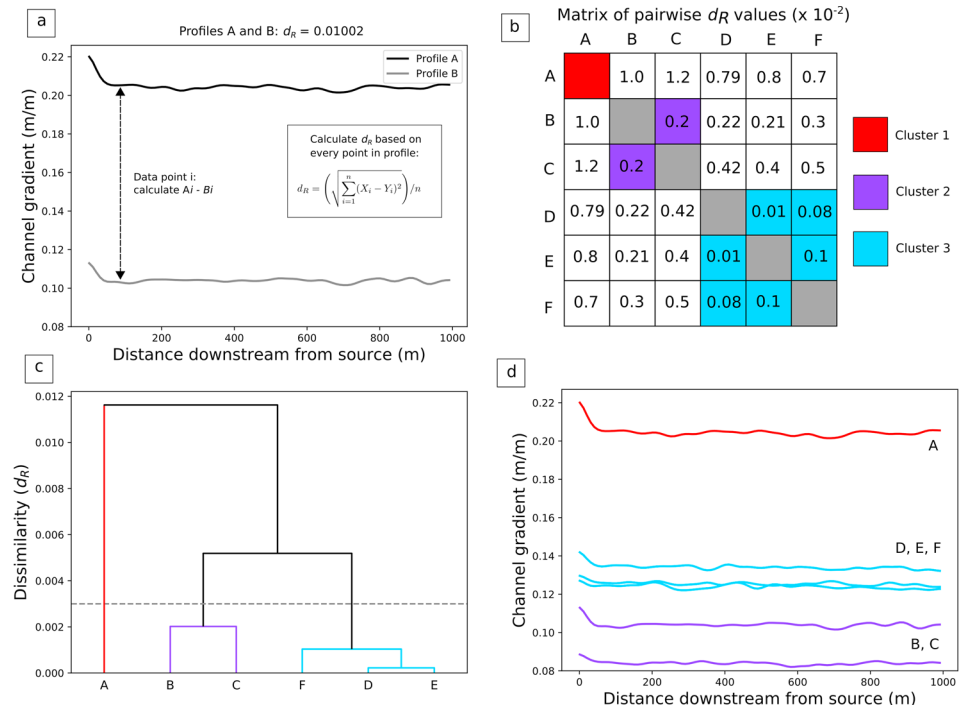


Figure 2. Schematic example of the clustering methodology. (a) We determine a dissimilarity between each pair of profiles following equation (4). This is shown schematically here for one pair of channel profiles. (b) We perform this calculation for every pair of profiles: for example, if we have six schematic river profiles labeled A to F, we calculate a six by six matrix where the values represent the dissimilarity (d_R) between each pair. We then use this dissimilarity matrix as an input to the clustering. Colors represent the d_R values resulting in the eventual clusters in following panels. (c) Hierarchical clustering is then performed on the dissimilarity matrix, leading to a dendrogram showing each profile is related to every other one, where the distance of each link on the Y axis represents the dissimilarity (d_R) between the profiles. In this schematic example we find three distinct clusters colored red, purple, and blue. Dashed gray line corresponds to cutting of the dendrogram explained in Figure 3. (d) We then use the dendrogram to assign our six original channel profiles to the corresponding cluster.

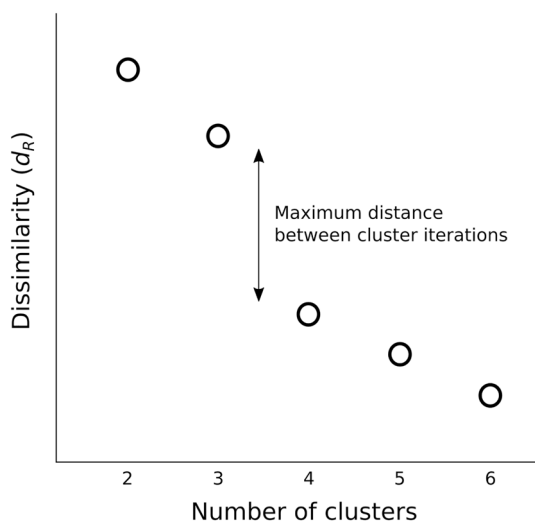


Figure 3. We select an appropriate number of clusters by plotting the number of clusters versus the distance in dissimilarity space between the center of each cluster and selecting the number of clusters where there is the maximum distance increase after a cluster is created. This allows us to “cut” the dendrogram at a level with the most distinct clustering, shown by the gray dashed line in Figure 2c. In this schematic example the maximum distance occurs when we go from four to three clusters, and we would therefore select three clusters as the most appropriate cutoff point.

in a dendrogram (Figure 2c) showing how each of the profiles is related to every other one. This clustering is performed between the river profiles in profile dissimilarity space (d_R) and is not related to the geographic location of the channel networks (Figure 2d).

After the clustering is complete, we must then determine a dissimilarity threshold which will select the final number of clusters, or the “level” at which to cut the dendrogram. In order to do this, we plot the dissimilarity (d_R) between clusters against the number of clusters at each iteration and then pick the number of clusters where the change in distance between two iterations is greatest (Figure 3). This allows us to select the iteration with the most distinctive clusters. This criteria often tends to result in a small number of clusters, and therefore, we also provide the results with the second greatest change in distance between two iterations as default within our algorithm. When applying the algorithm, users should combine the results of the clustering with knowledge of the geomorphology of a site, such as lithological variations, knickpoint locations, or field information about channel profile morphology, to determine the most appropriate number of clusters.

3.3. Extraction of Channel Steepness Estimates

We demonstrate one potential application of our technique by extracting channel steepness estimates using logarithmic plots of slope against drainage area following the clustering. Although many other techniques for estimating channel steepness exist, such as integral profile analysis, we choose here to focus on slope-area analysis as it is still very widely used within the literature, and the concavity index can be directly calculated from the data based on equation (1). However, we note that users of our clustering technique could choose any method of extracting channel steepness after clustering.

We extract channel steepness from each cluster by performing slope-area analysis separately on the channels in each cluster. When running the clustering algorithm, we use only first-order channels in order to ensure we compare a similar range of drainage areas (section 3.1 and Table 1). However, slope-area analysis requires a large range of drainage areas (i.e., several orders of magnitude) in order to fit an appropriate power law following equation (1). Therefore, we tag each higher-order channel node according to the cluster of every source, which drains into it (i.e., a second-order channel with two tributaries would have two cluster identifiers). Higher-order channels are then only included in the slope-area analysis if all first-order tribu-

This division by n means that comparisons between longer profiles will result in a lower dissimilarity than shorter profiles, such that our method gives more weight to longer channel tributaries where we have more data to use for comparison. Equations (3) and (4) require that the profiles in each pair are the same length. We therefore compare the lengths of the profiles, starting at the channel head, and only perform the clustering over the length of the shortest of the two profiles in each pair. This means we remove part of the profile at the downstream end of the longer profile in each pair.

The calculation of this dissimilarity between every pair of profiles gives us a symmetric $n \times n$ matrix (Figure 2b), which we use as the basis for agglomerative hierarchical clustering. We cluster the data based on Ward’s method (Ward, 1963), also referred to as the minimum variance method. This algorithm iteratively merges clusters based on minimizing the distance (d) in profile dissimilarity space between a new cluster u , formed from two previous clusters s and t , and any other cluster v . The distance $d(u, v)$ is computed by

$$d(u, v) = \sqrt{\frac{n_v + n_s}{T} d(v, s)^2 + \frac{n_v + n_t}{T} d(v, t)^2 - \frac{n_v}{T} d(s, t)^2} \quad (5)$$

where n_s , n_t , and n_v are the number of profiles in clusters s , t , and v , respectively, and $T = n_v + n_s + n_t$. Readers are referred to Müllner (2011), Murtagh and Contreras (2012), and the SciPy hierarchy linkage documentation for more information. We note that Ward’s algorithm used here is the standard SciPy implementation, which is $O(n^2)$. This results

taries were within the same cluster. We remove any channel nodes with a drainage area less than 1,000 m² in order to ensure that we are only considering the purely fluvial portion of the network. We then logarithmically bin the data following the approach of Wobus et al. (2006) and fit a power law through the median of each bin based on equation (1), in order to extract the concavity index θ and the channel steepness index k_s . We can then use this calculated value of θ as a reference to calculate the normalized channel steepness (k_{sh}) for every point along the channel network using equation 2.

4. Testing on Synthetic Landscapes

We demonstrate the ability of our method to disentangle the effects of landscape heterogeneity on river profiles by first testing it on two numerical landscapes, created by a landscape evolution model based on detachment-limited stream power. This allows us to first demonstrate that the method works in a setting where the uplift and erosion history is fully constrained, and where we can explore a series of different scenarios for which we envisage the technique to be useful in future research. These scenarios are (i) a steady-state model with a lithological contact and (ii) a model simulating transient response of the fluvial network to sudden base level fall.

We ran a detachment-limited stream power model, based on Mudd (2016) and Mudd et al. (2018), where the model elevation evolves through time as

$$\frac{\partial z}{\partial t} = U - KA^m S^n, \quad (6)$$

where U is the uplift rate, K is channel erodibility, which is a measure of the efficiency of the incision process, and m and n are constant exponents. We solved for fluvial incision using the Fastscape algorithm of Braun and Willett (2013). In order to ensure computational efficiency, we did not include other processes, such as hillslope sediment transport, in the model. First, we created an initial model domain with a height of 2 km and a width of 4 km, and initialized it with a parabolic surface. The model has a grid resolution of 1 m, comparable to that of the real landscapes (see section 5). The north and south boundaries of the domain have a fixed elevation of 0 and the east and west boundaries are periodic. We then used a diamond-square fractal algorithm to generate the initial surface (Fournier et al., 1982), as we found that this provides the most realistic initial drainage patterns. We then ran the model for 800,000 years to fully dissect the landscape with an initial uplift rate of 0.0004 m/year, $K = 0.0005 \text{ year}^{-1}$, $m = 0.5$, and $n = 1$.

4.1. Spatially Varying Erodibility

After the creation of this initial numerical landscape, we selected a large catchment from the model domain, which was used as the starting topography for each of the model runs. This allowed us to ensure a realistic drainage network as well as long enough channels to ensure nonspurious clustering. We ran this starting topography, including surrounding catchments to avoid edge effects on our example catchment, for a further 800,000 years to ensure it had reached steady state, which we define as a variation in elevations of less than 0.01 mm between two successive time steps. Our first scenario is designed to simulate a very simple vertical lithological contact across a catchment. We therefore then increased the erodibility of the southern half of the model domain by 5 times that of the northern half of the domain, and ran the model for a further 800,000 years at the same uplift rate (see Video S1 in the supporting information), until another steady state was reached. This resulted in a total run time of 2.4 million years. We then ran the clustering algorithm on one basin from the domain which drains both the harder lithology to the north, and the softer lithology to the south (Figure 4a).

The clustering grouped the profiles in two distinct clusters, which directly correspond to the lithology variation: all of the first-order profiles in the harder lithology are grouped together, and separately from all of the first-order profiles in the softer lithology. The clustering dendrogram (Figure 4b) shows that this separation occurs at a large distance compared to the variations within each cluster, suggesting that this grouping is the most robust. We also plotted slope-area data separately for the profiles in each cluster (Figure 4c), which allows us to extract an order of magnitude difference in channel steepness between the cluster in the softer lithology ($k_s = 0.63$, $\theta = 0.5$) and the harder lithology ($k_s = 9.43$, $\theta = 0.64$).

4.2. Base Level Fall

Our second model scenario is a simple approximation of a base level fall event, such as a sudden drop in sea level, which causes transient response of the river network through knickpoint propagation. We started

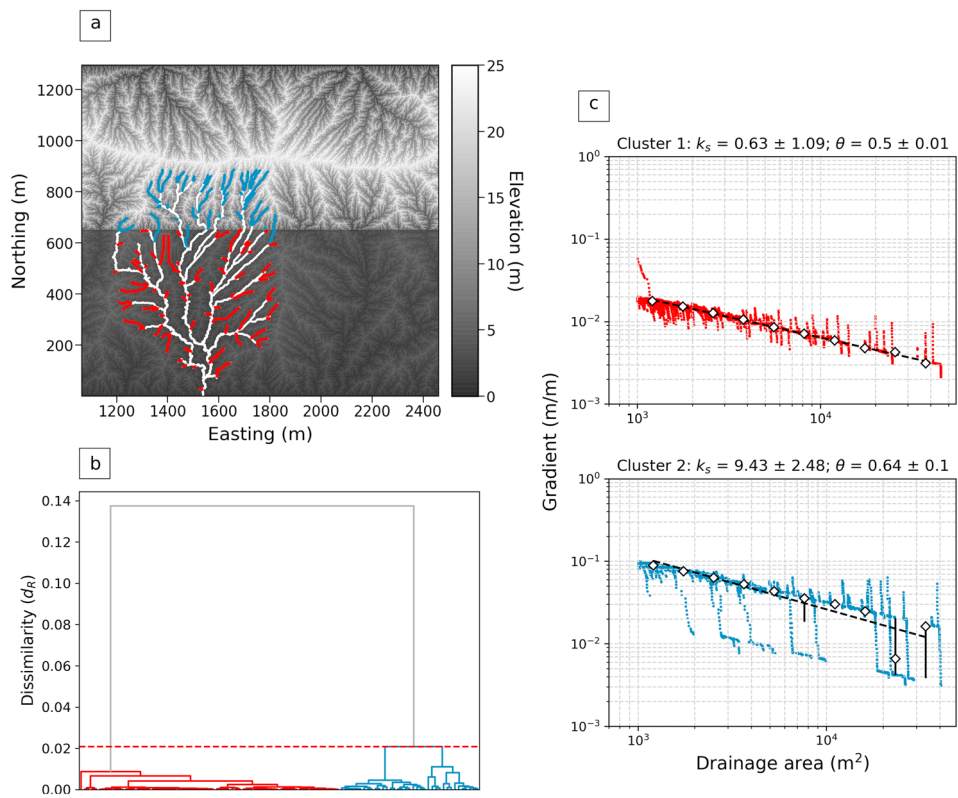


Figure 4. Results from the clustering of the numerical modeling run with spatially varying K , where the north half of the raster has lower erodibility (harder rocks) than the south half. (a) Elevation of model domain where dark gray is low elevation and white is high elevation. The river network from one catchment is shown with clustering of first-order streams, where the rest of the network is shown in white (not used for clustering). First-order streams are colored by cluster. (b) Hierarchical clustering dendrogram showing classification of all profiles into two distinct clusters, a red cluster (1) and a blue cluster (2). (c) Slope-area plots for the profiles separated by cluster. A linear regression through the log-binned data (white diamonds show the median, error bars represent the interquartile range) allows the extraction of k_s for each cluster: k_s in the blue cluster is an order of magnitude higher than in the red cluster. We report k_s and θ plus and minus the standard error on the regression coefficients.

our model run using the same initial topography as from the spatially varying erodibility scenario and ran for 800,000 years until steady state was reached. We then dropped the elevation of model base level nodes instantaneously by 10 m (simulating sudden sea level drop) and then ran with the same parameters for another 50,000 years. The model transiently responds by propagating a steepened reach up to the headwaters (see Video S2). We expected that this model scenario would be more challenging for our clustering algorithm than the spatially varying erodibility scenario. The channels above and below the location of the knickpoint should have similar gradients, and the location of the perturbation will change depending on the length of each channel. This will lead to significant variability in the downstream gradient profile of each channel, resulting in more noise in the clustering.

Figure 5 shows the results of our clustering algorithm on the transient run after 10,000, 30,000, and 50,000 years. In order to ensure that the clustering results are consistent through the model time steps, we cut the dendrogram at a constant dissimilarity threshold for each time step ($d_R = 0.1$). At 10,000 years, shortly after the base level fall, the vast majority of the profiles cluster together with just one profile in a separate cluster, as the transient signal has not yet propagated into any first-order channels. The long profile of the trunk channel suggests that the transient signal is at a distance of around 200–600 m from the outlet of the basin. The median profiles from this time step (Figure 5b) shows that these profiles are generally low gradient, with the red cluster representing one short outlier.

After 30,000 years, three distinct clusters emerge, colored red, blue, and black in Figures 5d and 5e. The profiles in the red and black clusters generally occur in the lower to middle region of the catchment. The

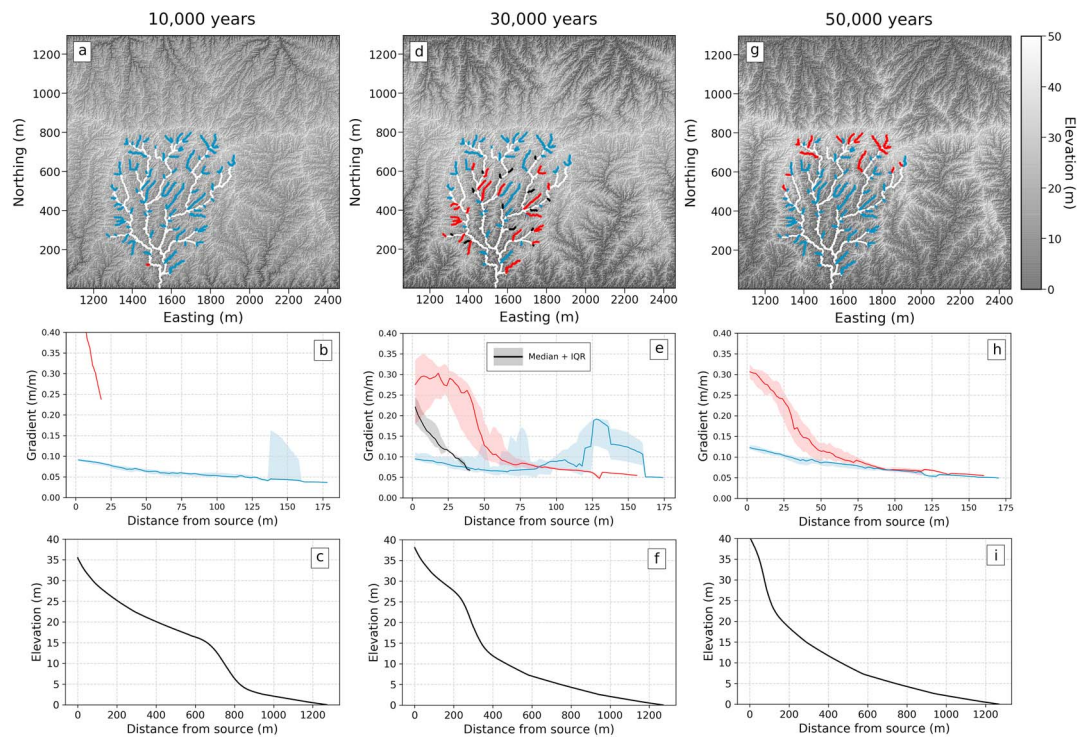


Figure 5. Results from the clustering of the numerical modeling run simulating instantaneous base level fall of 10 m. The top row shows elevation of the model run at different time steps, where the first-order streams are colored by cluster and the rest of the channel network is shown in white. The middle row shows the median channel profile for each cluster, plotted as gradient against distance from the source (m). The shaded area represents the interquartile range (IQR). The bottom row shows the long profile of the trunk channel at different time steps. (a–c) 10,000 years; (d–f) 30,000 years; (g–i) 50,000 years after base level fall event.

red cluster is characterized by elevated gradient in the headwaters, which persists until around 50-m downstream of the channel head. Profiles in the black cluster also have similarly elevated gradient in their headwaters but are generally shorter, with a length of around 40 m (Figure 5e). The elevated gradient in the headwaters of both of these clusters suggest that they are transiently responding to the base level change. The profiles in the blue cluster, on the other hand, are mostly located in the headwaters of the catchment where transient adjustment has not yet occurred. Many of the shorter first-order channels near the outlet of the catchment also fall into the blue cluster. The median gradient-distance profiles for this cluster show that these channels have low gradient in the headwaters, and slightly elevated gradient further downstream (around 120–160 m from the channel head). The long profile of the trunk channel for this time step (Figure 5f) shows that the transient perturbation is located around 800–1,000 m from the outlet, and that the profile below this point has returned to a steady-state concave form. We may therefore conclude these small channels near to the outlet are fully adjusted to the transient signal, and therefore, the gradient profile will be morphologically similar to those unaffected channels in the headwaters.

In the final model time step (50,000 years), two distinct clusters are once again detected, a larger blue cluster and a smaller red cluster. The smaller red cluster exclusively consists of channels in the headwaters of the model catchment, whereas all channels further downstream cluster together in blue. The long profile of the trunk channel (Figure 5i) shows that the transient signal has reached the upstream portion of the channel network (1,100–1,200 m from the outlet), suggesting that the red cluster represents the channels that have not yet fully readjusted after the transient perturbation. This interpretation is supported by the median gradient-distance profiles for this time step (Figure 5h), which shows that profiles in the red cluster are steep in their headwaters until around 75 m from the channel head, whereas the median profile of the blue cluster is lower gradient for the entirety of its length. Slope-area plots of the model time steps can be found in the supporting information (Figure S1).

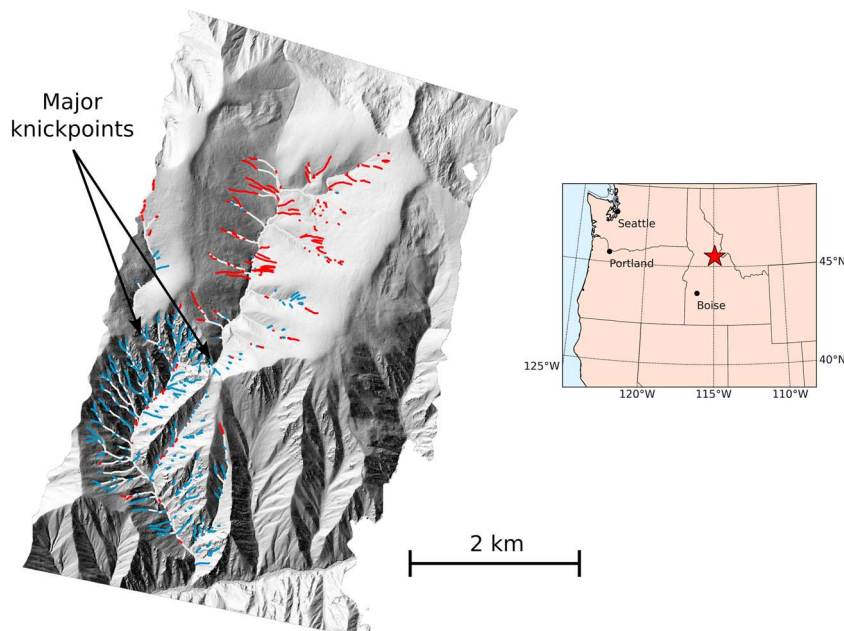


Figure 6. Shaded relief map of Harrington Creek, Idaho, showing results of the clustering algorithm. The first-order streams are colored by their identified cluster, and the rest of the channel network is shown in white. Center of the catchment is located at 45°31'03"N, 114°55'32"W (WGS84). Inset map shows location of Harrington Creek (red star).

5. Application to Real Landscapes

Following the demonstration that our method can successfully distinguish both variations in erodibility and transient perturbations in synthetic landscapes, we applied our clustering to two test sites with high-resolution topographic data (1-m resolution), to provide examples of real-world scenarios in which landscape heterogeneity can be detected.

5.1. Harrington Creek, Bitterroot National Forest, Idaho

Our first test site is a region with evidence of recent fluvial incision and transience through the preservation of major knickpoints. Harrington Creek is a small tributary of the Salmon River, Idaho, where recent incision has resulted in the propagation of knickpoints through its tributaries (Wood, 2013). This knickpoint propagation has led to a stark contrast between the low relief, relict landscape in the headwaters of the Harrington Creek catchment, and the steeper, more rapidly eroding downstream portion below the knickpoint (Figure 6). The landscape below the knickpoint displays a marked increase in drainage density (Clubb et al., 2016) and more frequent bedrock outcrops (Milodowski et al., 2015) compared to the relict landscape. The lithology is relatively homogeneous, consisting of plutonic rocks of the Idaho Batholith with some minor Eocene rhyolitic-dacitic dykes (Lewis & Stanford, 2002). The lidar data for the site were collected by the National Center for Airborne Laser Mapping (NCALM) with an original point density of 4.6 pts/m², gridded to a 1-m bare-earth DEM.

We use this test site to demonstrate the ability of our method to (i) map transient incision waves throughout landscapes and (ii) distinguish the impact of different geomorphic process regimes on channel profiles. First, we perform the clustering analysis on all first-order channels using the same parameter values as for the synthetic landscapes (Table 1). Figure 6 shows the spatial distribution of first-order channels colored according to their assigned cluster. We cut the dendrogram using the maximum distance between clusters (Figure 3), which results in two main clusters. The spatial distribution of the first-order profiles in each cluster clearly identifies the main knickpoint in the catchment, where the majority of the profiles in the red cluster (87% of channel pixels) are located above the knickpoint in the relict landscape and the majority of the profiles in the blue cluster (89% of channel pixels) are located below the knickpoint in the incised landscape.

The dendrogram of the Harrington Creek river profiles shows that the two clusters are distinct from each other in dissimilarity space (Figure 7a), with the threshold occurring at $d_R = 0.7$. The median gradient of

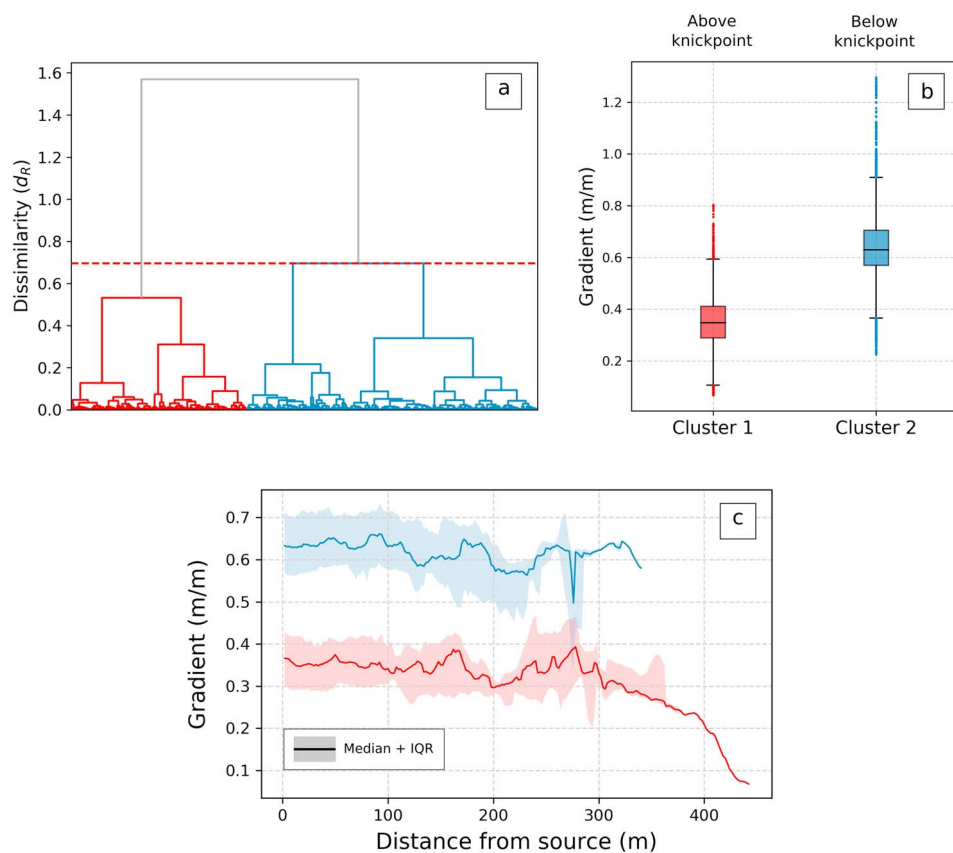


Figure 7. Results of the clustering algorithm for Harrington Creek, Idaho. (a) Hierarchical clustering algorithm showing distinct separation of profiles into two clusters, a red cluster and a blue cluster. (b) Box-and-whisker plot showing the distribution of channel gradient for each cluster. The solid black line represents the median, the edges of the box are the interquartile range (IQR), and the whiskers represent 1.5 times the IQR. The colored points outside of the whiskers are outliers. (c) Plot showing the median (solid line) and the interquartile range (shaded area) of gradient against distance downstream from the channel head for each cluster. The red cluster mainly consists of channels in the relict landscape above the knickpoint, whereas the blue cluster mainly consists of channels in the steeper landscape below.

profiles in the red cluster is much lower than that of the blue cluster (0.35 ± 0.12 m/m compared to 0.63 ± 0.14 m/m, Figure 7b, errors represent the interquartile range), and the median gradient-distance profiles for each cluster (Figure 7c) show that the channels in the blue cluster have a consistently higher gradient along the entirety of the first-order profile.

We demonstrate the ability of the method to disentangle the impact of different geomorphic processes on valley networks by plotting the slope against drainage area separately for each cluster (Figure 8a). We find that the slope-area data for each cluster results in the calculation of low concavity values ($\theta = 0.14 \pm 0.03$ for the red cluster above the knickpoint, and $\theta = 0.04 \pm 0.01$ for the blue cluster below the knickpoint). This is consistent with the median slope-distance profiles for each cluster (Figure 7c), which show a generally invariant gradient with distance along the first-order profiles for the first 300 m downstream of the channel head. Previous work by Stock and Dietrich (2003) found that low concavity values can indicate valley incision by mass wasting processes, such as debris flows. The data included in the slope-area calculations for each cluster spans from drainage areas of $1,000 \text{ m}^2$ to 1 km^2 (we include data from higher-order streams within the same cluster when performing the slope-area analysis, as outlined in section 3.3). We then performed the clustering on the longest channel in each third-order basin ($S_o = 3$) and again plotted the slope-area data for each cluster (Figure 8b). We find that profiles included in the blue cluster of third-order profiles again span drainage areas up to 1 km^2 and have a similarly low concavity to the clustering over the first-order channels ($\theta = 0.06 \pm 0.02$). The red cluster, however, includes profiles up to a drainage area of 10 km^2 and has a higher concavity. If we calculate θ by excluding drainage areas lower than 1 km^2 , we obtain $\theta = 0.51 \pm$

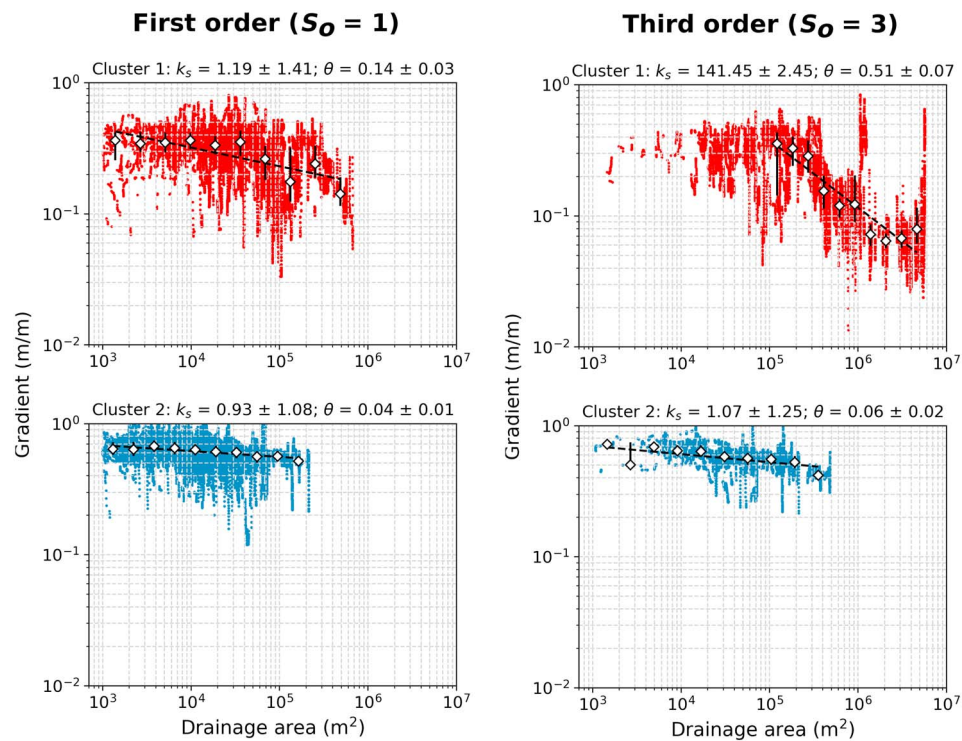


Figure 8. Slope-area plot for Harrington Creek when clustering over first-order channels (left column, $S_o = 1$) and third-order channels (right column, $S_o = 3$). The channel steepness k_s and concavity θ are calculated by log-binning the raw data (white diamonds show the median, error bars represent the interquartile range), and then calculating a least squares fit through the log-binned data. We report k_s and θ plus and minus the standard error on the fitted coefficients. We find a low concavity for both clusters when $S_o = 1$, whereas when $S_o = 3$ we find a higher concavity in the red cluster ($\theta = 0.51 \pm 0.07$) at higher drainage areas (we exclude drainage areas less than 1 km^2 from the fit for the red third-order cluster).

0.07. We therefore suggest that the valley network with a drainage area greater than 1 km^2 is fluvially dominated, whereas lower drainage areas are more influenced by mass wasting processes. This highlights how the clustering technique can be used to understand the dominant controls on valley network incision.

Another potential advantage of our clustering approach is the ability to segment the landscape into different regions depending on the similarity of the river profiles. To demonstrate this, Figure 9a shows the catchment area associated with each first-order channel separated by its assigned cluster. This separation of drainage basins by the clustering of their channel profiles allows us to examine how local gradient and catchment relief vary in each cluster (Figure 9). We calculate the local gradient by fitting a second-order polynomial surface with a radius of 7 m, following Hurst et al. (2012). We calculate catchment relief as the maximum elevation minus the minimum elevation within each catchment, normalized for the area of the basin. In our Harrington Creek site we find that both the median local gradient and the normalized catchment relief are lower in the red cluster above the knickpoint ($0.36 \pm 0.14 \text{ m/m}$ and $0.018 \pm 0.022 \text{ m/m}^2$ respectively, errors represent the interquartile range) compared to the blue cluster below the knickpoint ($0.77 \pm 0.26 \text{ m/m}$ and $0.028 \pm 0.031 \text{ m/m}^2$, respectively), mirroring that of the channel profiles (Figure 7b). We report the Kolmogorov-Smirnov D statistic on the distributions in each cluster (see Figure 9b) to test whether they are significantly different and find we can reject the null hypothesis that they come from the same distribution at a 99% confidence level. This example shows how the clustering technique can be used to separate and analyze the signature of transient incision waves throughout the landscape.

5.2. Pozo Catchment, Santa Cruz Island, CA

Our second test site is from a landscape with a complex tectonic history as well as spatial variations in lithology: the Pozo catchment, a small catchment on Santa Cruz Island in the California Channel Islands. The Pozo catchment is located in the southwest of the island (Figure 10) and has a drainage area of around 6.5 km^2 , with an average basin relief of 400 m. Santa Cruz Island, and the Pozo catchment in particular,

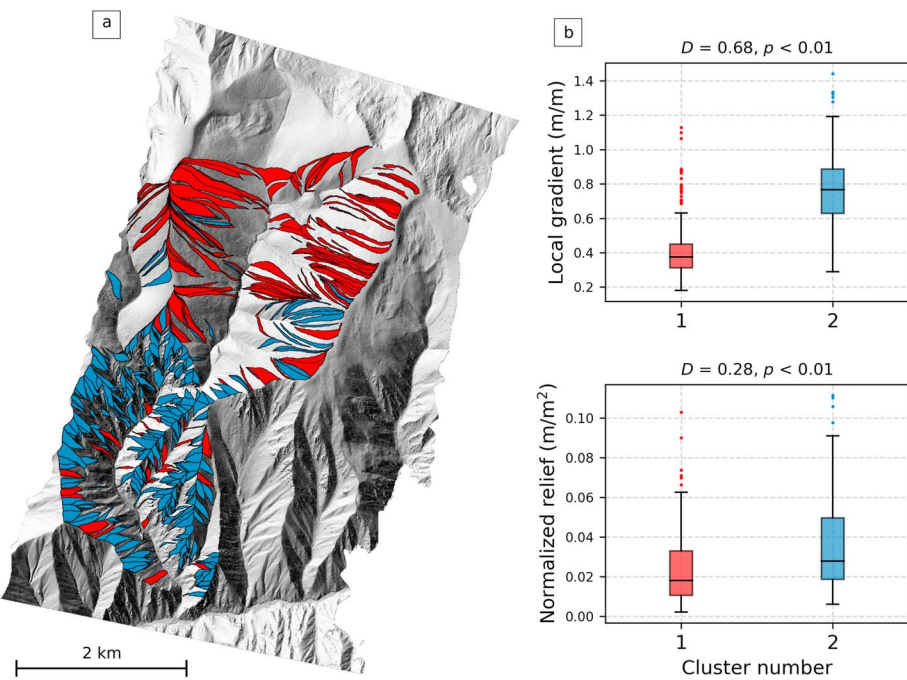


Figure 9. (a) First-order catchments of Harrington Creek, Idaho, colored by the clustering of the channel in each basin. (b) Boxplots of mean local gradient and relief for each cluster. We report the catchment relief as the maximum minus the minimum elevation for each basin, normalized by the area of the basin. We report the Kolmogorov-Smirnov D statistic to compare the distributions for each metric and find that we can reject the null hypothesis that they come from the same distribution at a 99% confidence level.

experienced intensive gullying, vegetation loss, and soil erosion in the late nineteenth and early twentieth century (Perroy et al., 2010). The geology of the Pozo catchment can be split into three main geologic units: a lower unit consisting of a Tertiary sedimentary succession, the main formation of which is referred to as the Canada shale; a middle unit consisting of the San Onofre breccia; and an upper unit consisting of the more resistant Blanca volcanics (Dibblee, 2001; Perroy, 2009). The Canada shale is the weakest lithology in the basin, and therefore, the majority of the erosion occurred within this unit (Perroy et al., 2010). Figure 11 shows the surface expression of the shale lithology, including the development of extensive gullying. Hillslope relief is generally higher in the San Onofre breccia and Blanca volcanics compared to the Canada formation, which mostly consists of shallow ridges and smooth hillslopes (Figure 11). The Pozo catchment has cosmogenic-nuclide basin wide erosion rates of 0.08 mm/year (Perroy et al., 2012). Alongside this lithological variation, Santa Cruz Island is currently uplifting at around 0.1 mm/year, resulting in the preservation of knickpoints, hanging valleys, and marine terraces (Muhs et al., 2014; Neely et al., 2017; Pinter et al., 1998).

The digital elevation data for the Pozo catchment were obtained from the 2010 US Geological Survey Channel Islands Lidar Collection, and the original point cloud was gridded to a 1-m bare-earth DEM, with an average point density of 10 pts/m². We extracted the river network and performed the clustering analysis on the first-order channels using the methodology detailed in section 3, identical to that used on the model landscapes. We kept the user-defined parameters identical to that of the model runs (Table 1). Figure 12 shows the results of the method for the Pozo catchment compared to the lithological data. When we cut the dendrogram using the maximum dissimilarity approach ($d_R = 0.9$), we find two main clusters, colored red and blue in Figure 12a. The vast majority of the profiles in the red cluster fall within the weaker Canada shale unit (95% of channel pixels), whereas the majority of the profiles in the blue cluster are located within the other, more resistant lithologies (78% of channel pixels).

Examining the dendrogram for the Pozo catchment (Figure 13a) shows that the next largest dissimilarity threshold would result in three clusters: the red cluster would be preserved and the blue cluster would be split into two at $d_R \approx 0.7$. However, the spatial location of the further clustering is unable to distinguish between the volcanoclastic lithologies, although the difference between the Canada shale and the volcani-

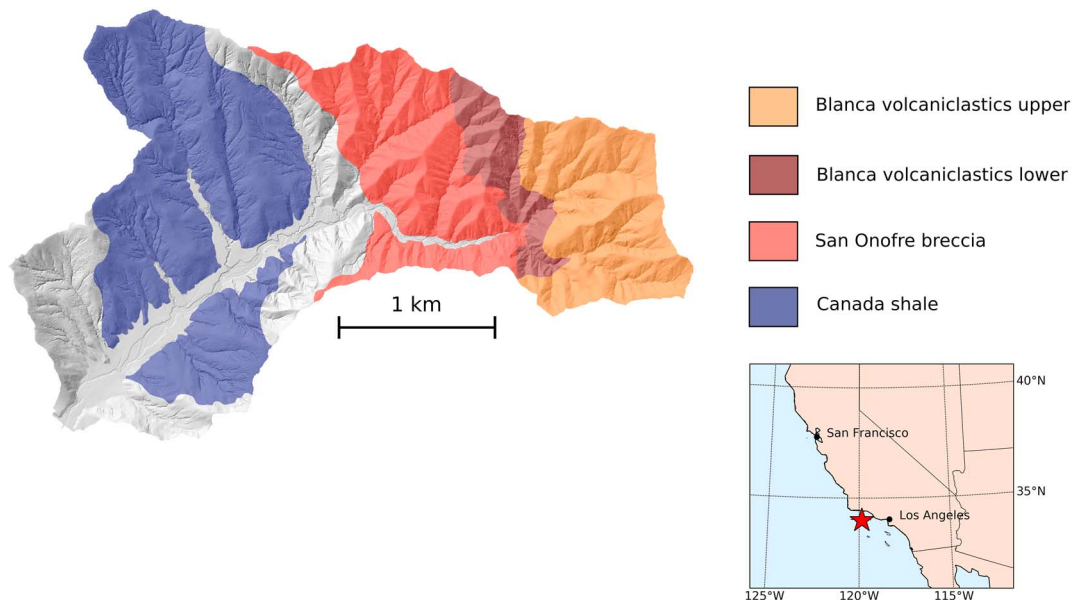


Figure 10. Shaded relief map of the Pozo catchment, Santa Cruz Island, CA, draped with main lithological units from Dibblee (2001). The Canada shale (purple) is a weak, poorly consolidated unit with extensive gullying, compared to the San Onofre breccia and the Blanca volcaniclastics (warm colors), which are more resistant. Center of the catchment is located at $33^{\circ}59'18.2''\text{N}$, $119^{\circ}51'03.8''\text{W}$ (WGS84). Inset map shows location of Santa Cruz Island offshore of California.

lastic units is still preserved (Figure 12b). We find that the median gradient of the profiles in the red cluster primarily located in the shale is $0.28 \pm 0.13 \text{ m/m}$, compared to a higher median gradient of $0.46 \pm 0.17 \text{ m/m}$ in the blue cluster in the volcaniclastics (Figure 13b, errors represent the interquartile range). Examining the median gradient-distance profiles for the two clusters (Figure 13c) shows that in the blue cluster, the gradient is highest in the headwaters and decreases as a function of distance downstream, following a typically fluvial profile as described by Flint's law (equation (1)). In the red cluster, however, the channel gradient does not systematically decrease in the downstream direction, instead appearing relatively constant for the first 100 m downstream of the channel head. Invariant gradient with distance has previously been suggested to be indicative of erosion by mass wasting processes, such as debris flows (Stock & Dietrich, 2003). Therefore, we suggest that the constant gradient in the headwaters of the red cluster represents the signature of extensive gullying within the Canada shale (e.g., Perroy, 2009, 2010, 2012), which can be seen in Figure 11.

We also demonstrate the potential of the clustering approach for segmenting the landscape by analyzing the first-order catchments associated with each cluster, following the same approach as for the Harrington Creek site. We calculate the distribution of local gradient and normalized catchment relief in each clus-

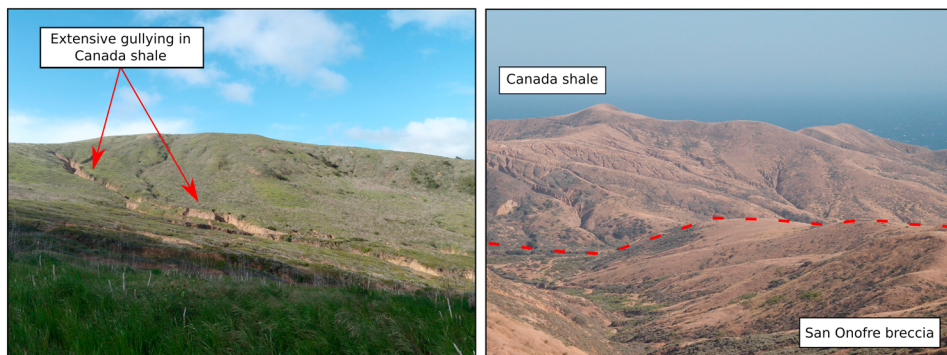


Figure 11. Field photographs showing the surface expression of the different lithologies. (a) The Canada shale unit contains extensive gullying with smooth, diffusive hillslopes; (b) dashed red line represents boundary between the Canada shale in the background and the San Onofre breccia in the foreground. The San Onofre breccia and Blanca volcaniclastics result in less gullying, but steeper hillslopes than the Canada shale.

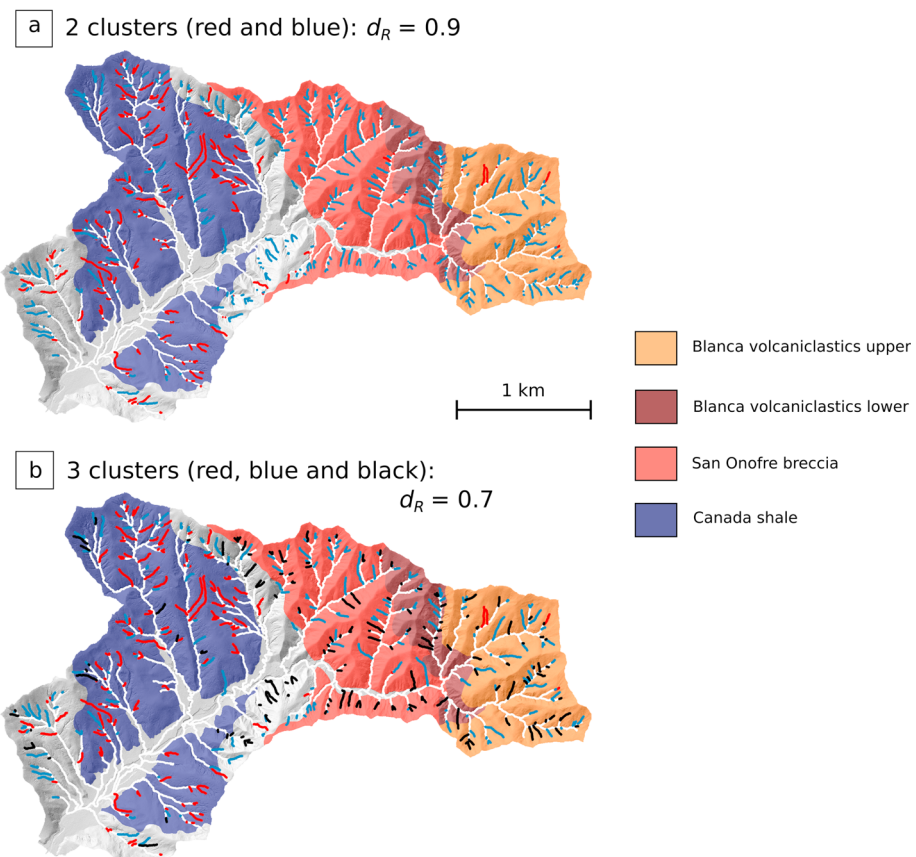


Figure 12. Shaded relief and lithology map of the Pozo catchment compared to the results of the clustering algorithm. The first-order streams are colored by their identified cluster, and the rest of the channel network is shown in white. (a) Dendrogram is cut at the greatest dissimilarity between clusters ($d_R = 0.9$), resulting in two clusters. (b) When the second threshold is used (second greatest dissimilarity, $d_R = 0.7$) three clusters are selected.

ter (Figure 14) and find that the medians of both metrics are significantly lower in the red cluster (mostly Canada shale, 0.36 ± 0.12 m/m and 0.013 ± 0.008 m/m² respectively; error represents the interquartile range) compared to the blue cluster (mostly volcaniclastics, 0.58 ± 0.16 m/m and 0.02 ± 0.014 m/m², respectively). We also compare the vegetation height within basins in each cluster using a canopy height model derived from the lidar point cloud for the Pozo catchment. The canopy height model was calculated by first classifying all ground points and then measuring vegetation height above ground for each vegetation point. These were aggregated to 1-m spatial resolution by using the maximum vegetation height for each grid cell following methodology described in Khosravipour et al. (2014). We find that, although the median vegetation height within the red and the blue cluster are similar, the range of the distribution is much narrower within the red cluster compared to the blue cluster (Figure 14). This difference in vegetation height may also be due to the lithological contrast: the Pozo catchment was exposed to extensive anthropogenic erosion in the early twentieth century, which led to gullying and vegetation loss, which was more pronounced in the weaker Canada shale unit compared to the more resistant volcaniclastics (Perroy et al., 2010).

Finally, we demonstrate the ability of the clustering method to provide greater insights into controls on channel morphology by comparing it to a standard approach of calculating normalized channel steepness (k_{sn}) for the catchment. We plotted the slope-area data for the entire Pozo catchment and calculated a concavity index (θ) of 0.45 ± 0.02 following the approach detailed in section 3.3. Figure 15a shows the slope-area data for the Pozo catchment, from which it is difficult to determine any meaningful segment breaks that may correspond to landscape heterogeneity. We then used $\theta_{ref} = 0.45$ to determine k_{sn} for each point in the network, shown in Figure 15b. We find that variations in k_{sn} in the Pozo catchment generally correspond to transitions between the alluviated trunk channel and the surrounding tributaries. We then plotted the distribution of k_{sn} by lithology and found no significant variation in median k_{sn} between the different rock types

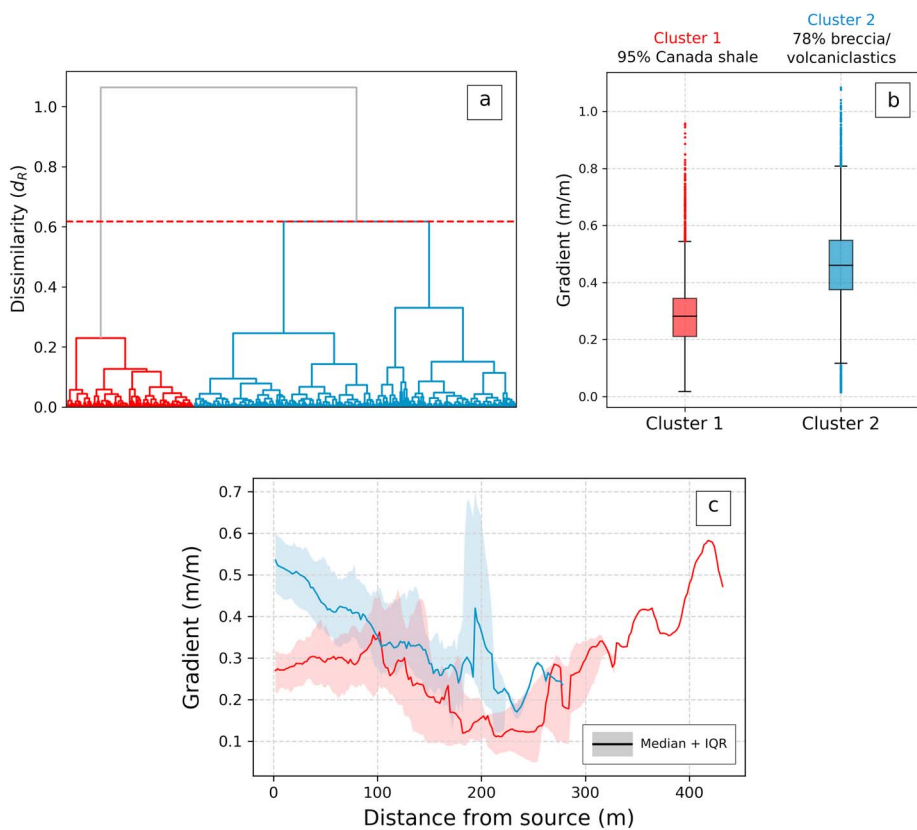


Figure 13. Results of the clustering algorithm for Pozo catchment, Santa Cruz Island. (a) Hierarchical clustering algorithm showing distinct separation of profiles into two clusters, a red cluster and a blue cluster. (b) Box-and-whisker plot showing the distribution of channel gradient for each cluster. The solid black line represents the median, the edges of the box are the interquartile range (IQR), and the whiskers represent 1.5 times the IQR. The colored points outside of the whiskers are outliers. (c) Plot showing the median (solid line) and the interquartile range (shaded area) of gradient against distance downstream from the channel head for each cluster. The majority of the red channels are in the Canada shale, whereas the blue channels are predominantly situated in the San Onofre breccia and the Blanca volcanics.

(Figure 15c). This demonstrates that the lithological distinction between the channel profiles identified by the clustering algorithm is not picked up simply by plotting k_{sn} throughout the catchment, most likely due to noise in the slope-area data in Figure 15a.

We then plotted the slope-area data for the profiles separately by cluster, in order to determine a representative channel steepness metric for each cluster (Figure 16). The channel steepness for the red cluster, primarily located in the Canada shale, is lower than that of the more resistant lithologies ($k_s = 3.59 \pm 1.46$, $\theta = 0.32 \pm 0.04$ compared to $k_s = 12.83 \pm 1.3$, $\theta = 0.41 \pm 0.03$, error represents standard error on the regression parameters). This demonstrates the ability of our clustering approach to improve estimates of both channel steepness and concavity: although the data for the catchment as a whole suggests $\theta = 0.45$, channels in the red cluster with the weaker lithology exhibit a lower concavity value of 0.32. We again suggest that this lower concavity value is due to the constant gradient in the headwater of these channels, which are predominantly affected by gullying.

6. Discussion

6.1. Caveats and Limits to Hierarchical Clustering

The examples above from both real and synthetic landscapes demonstrates the ability of the clustering method to identify groups of similar channel profiles in heterogeneous landscapes. However, care must be taken before applying the method to ensure that the results of the clustering are meaningful. For example, determining an appropriate number of clusters is generally a challenge for any study which uses clustering techniques (e.g., Aghabozorgi et al., 2015). One of the advantages of the hierarchical clustering approach

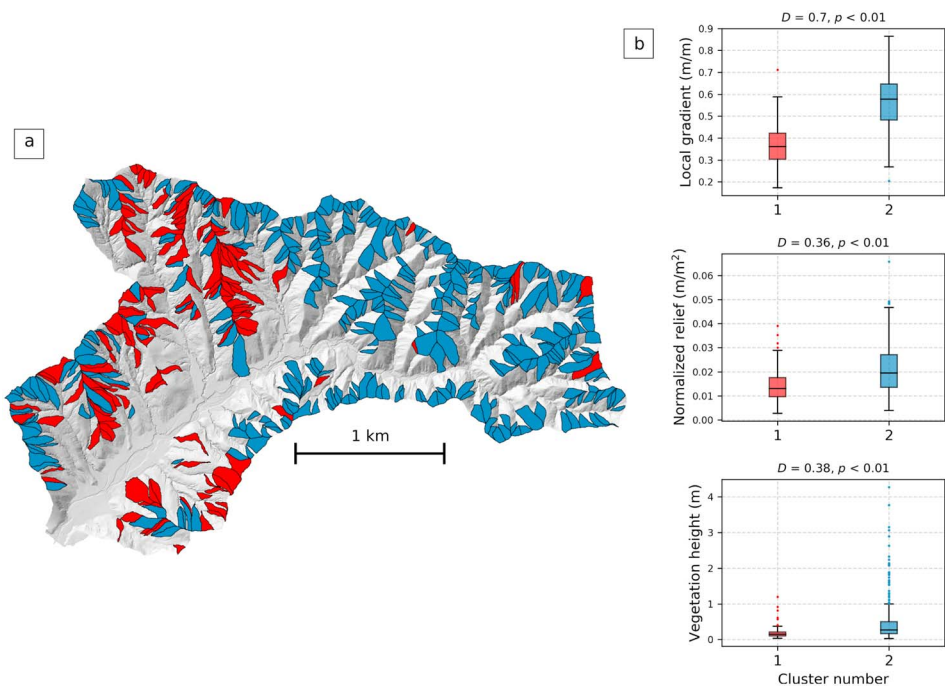


Figure 14. (a) First-order catchments of the Pozo catchment, colored by the clustering of the channel in each basin. (b) Boxplots of mean local gradient, relief normalized by basin drainage area, and vegetation height for each cluster. We report the Kolmogorov-Smirnov D statistic to compare the distributions for each metric and find that we can reject the null hypothesis that they come from the same distribution at a 99% confidence level.

that we take here is that it does not require the number of clusters to be set as an input parameter. The structure of the dendrogram (Figure 3a) can provide useful information regarding the relationship between all profiles, which can aid in determining an appropriate number of clusters. Here we take the approach of cutting the dendrogram at the greatest dissimilarity d_R between clusters (Figure 3b), which tends to lead to small numbers of clusters. Therefore, we also provide an additional level of clustering at the second greatest dissimilarity, shown in our example of the Pozo catchment in Figure 12. However, in principle there is no “incorrect” level at which to cut the dendrogram: this should depend on the scale over which the grouping is required.

We stress that it is essential to examine the dendrogram of the clustering along with a process-based understanding of the geomorphology of the region to determine the number of clusters. For example, the Harrington Creek test site shows that a selection of two clusters isolates the main transient incision wave within the catchment and is therefore the most appropriate for this landscape. In fact, this is one of the key advantages of the clustering approach: it is an exploratory, data-driven technique which can be compared to independent geomorphic information or data sets. It can be used in cases where, such as with river profiles, we may have a large number of data points and wish to explore potential signals among the noise of typically imperfect landscapes.

When applying the method, care must also be taken to appropriately set the four user-defined parameters. These parameters, along with suggested values for use with 1-m resolution gridded topographic data, are shown in Table 1. Throughout the analysis in this study we kept the parameters constant using these suggested values for both the synthetic landscapes as well as the real test sites. However, we caution that these parameters may need to be adjusted for other landscapes as well as for the resolution of the DEM that is used. For example, the window size W_s (Figure 1) will affect the number of nodes over which the channel slope is calculated, and therefore the gradient-distance profiles used as an input for the clustering. If W_s is too small, the channel slope will likely be influenced either by local roughness or by noise in the DEM and will not reflect the prevailing slope of the channel bed. However, if W_s is too large then real variations in the channel slope through features such as knickpoints may be smoothed out. Therefore users must carefully consider an appropriate reach length for the calculation of channel slope for the landscape and the resolu-

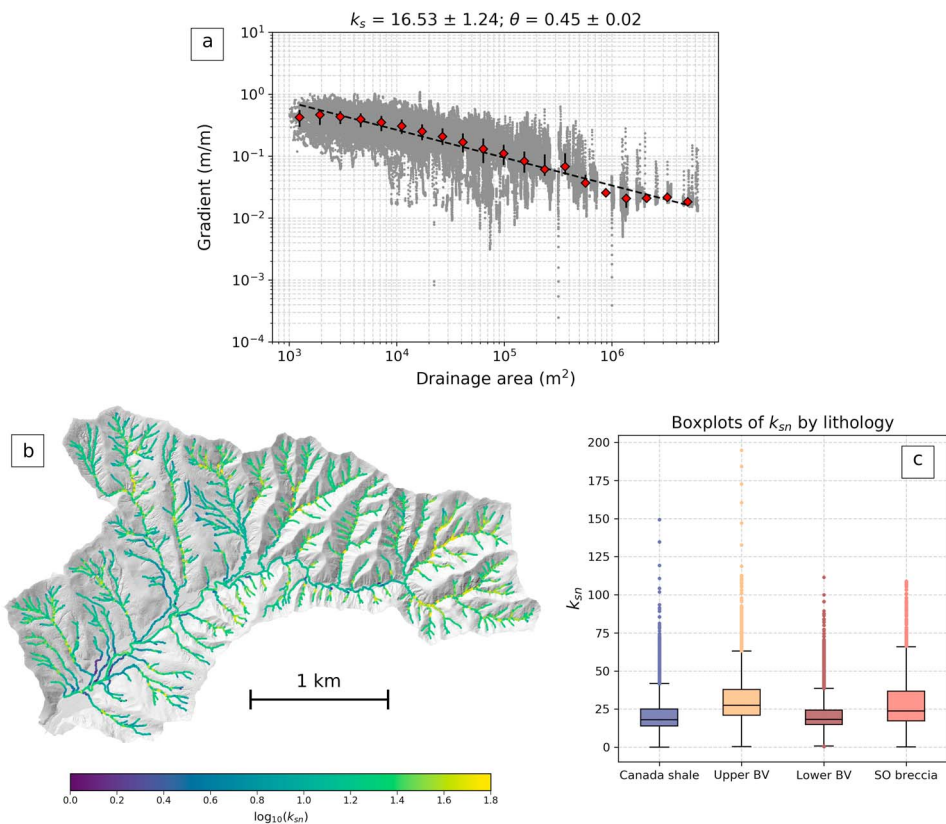


Figure 15. Normalized channel steepness analysis for the Pozo catchment. (a) Log-binned slope-area plot of the entire Pozo catchment (red diamonds show the median, error bars represent the interquartile range, IQR). We calculate θ as the exponent of a least squares fit through the log-binned data (0.45 ± 0.02). (b) Map of the normalized channel steepness k_{sn} with 0.45 as the reference concavity θ_{ref} . k_{sn} values are represented on a log color scale to highlight the relative differences. (c) Boxplots of the distribution of k_{sn} with each lithology (spatial distribution of the lithologies can be seen in Figure 10). There is little variation in the median k_{sn} with lithology (median and IQR values are 17.97 ± 11.16 for the Canada shale, 27.377 ± 16.92 for the upper Blanca volcaniclastics, 18.21 ± 9.49 for the lower Blanca volcaniclastics, and 23.76 ± 19.47 for the San Onofre breccia).

tion of the topographic data in question. We also set a minimum length of each profile to be included in the clustering (L_T), to ensure that each profile contains a sufficient number of data points to perform a meaningful clustering. In this study we set this to a small number of nodes $L_T = 5$, but users may wish to increase this value in order to filter out very short profiles and potentially reduce noise in the clustering results. For each example shown here we perform the clustering on first-order channels ($S_o = 1$). We found that a small stream order is able to best identify landscape heterogeneity, as it clusters over a finer spatial scale than using the entire channel profile from channel head to outlet, for example. However, we provide the option within our implementation of the algorithm for users to cluster over any number of stream orders that they wish: this allows the effective segmentation of the channel network into sections with similar drainage area, which can all be clustered independently. We also performed the analysis on Harrington Creek and the Pozo catchment for second-order channels (see Figures S2–S5 in the supporting information) and found similar patterns of clustering to that of the first-order channels.

6.2. Potential Applications

Our results from the synthetic landscapes (section 4) demonstrate the ability of the method to identify regions of landscape similarity in a setting where prior uplift and erosion histories are fully constrained. The first model example showed that our clustering technique was able to detect variations in erodibility in an otherwise steady state model setup. Performing channel steepness analysis on each cluster separately allowed us to extract an order of magnitude difference in k_s between the region with varying erodibility, highlighting an important potential application of the clustering technique in real landscapes. We then tested the technique on a synthetic landscape transiently adjusting to a sudden base level fall event and found

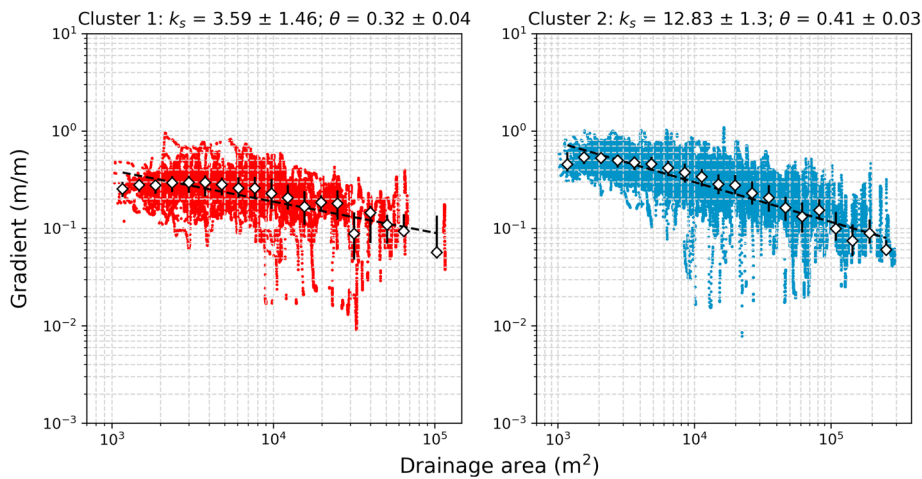


Figure 16. Slope-area plots for the Pozo catchment by cluster. The channel steepness k_s and concavity θ are calculated by log-binning the raw data (white diamonds show the median, error bars represent the interquartile range), and then calculating a least squares fit through the log-binned data. We report k_s and θ plus and minus the standard error on the fitted coefficients. The fitted concavity for the red cluster ($\theta = 0.32 \pm 0.04$) within the weaker lithology is lower than that of the blue cluster ($\theta = 0.41 \pm 0.03$) and the Pozo catchment as a whole ($\theta = 0.45 \pm 0.02$).

that clustering of the first-order channels allowed the spatial and temporal mapping of this transient signal through the river network. Our technique allows the extraction of a ‘characteristic’ profile of gradient against distance downstream for each cluster (Figures 5b, 5e, and 5h), which clearly show the separation of the first-order profiles into those which are steady state and those which are transient. These synthetic landscapes are by nature simplistic, as they only include detachment limited stream power with no hillslope diffusion or simulation of landsliding processes, for example. We therefore expected that clustering of river profiles in real landscapes would be more challenging due to the wide variety of geomorphic processes and landscape heterogeneity which is not captured in these model runs. However, they are useful indications of potential real-world situations in which the clustering technique could be applied.

Following on from these synthetic examples, we then highlight the ability of the clustering technique to identify landscape similarity in two real-world scenarios. We show that in transient landscapes, such as in Harrington Creek, our method can be used to identify parts of the landscape responding to different erosion rates, for example. The results from Harrington Creek (Figure 6) show that the channels in the relict landscape above the knickpoint cluster separately from those in the steeper landscape below the knickpoint, allowing the spatial mapping of transient signals. We find that the median channel gradient of the first-order channels in the cluster below the knickpoint is nearly double that of the channels above the knickpoint (0.63 compared to 0.35, respectively). Furthermore, the median gradient-distance profile for each cluster shows that this difference in gradient is maintained consistently from the headwaters to the downstream tributary junctions of the first-order channels. These aggregated statistics of each cluster therefore provide a useful indicator of the overall difference in channel profile gradient between clusters as well as any spatial pattern within each cluster. We then plot slope-area data separately by cluster, as well as comparing the clustering of first-order to third-order channels to identify the topographic signature of different geomorphic processes in the landscape. We found that clustering over third-order channels led to the separation between channels with both low drainage areas and low concavity, indicative of valley incision by debris flows (e.g., Stock & Dietrich, 2003), and channels with higher drainage area and concavity indicative of fluvial incision. This highlights how clustering can be used to objectively analyze geomorphic process domains within the valley network.

Our method also allows potential identification of the main factors affecting channel profile morphology. For example, in the Pozo catchment, the results of the clustering were primarily correlated to lithological variations between a weaker, unconsolidated shale unit compared to more resistant volcaniclastics. This lithological impact on the river profiles persists despite evidence for propagation of transient signals from sea level changes through the catchment, such as the preservation of knickpoints, hanging valleys, and marine terraces (Neely et al., 2017), as well as recent anthropogenic erosion (Perroy, 2009, 2010). Although

we perform the clustering based on the channel profiles, our analysis need not be restricted to purely river profile analysis: we also extracted the catchments associated with each cluster, allowing us to compare landscape relief and gradient across each cluster, as shown in Figures 9 and 14. This demonstrates the ability of the clustering method to spatially segment the landscape into areas with morphological similarity. Furthermore, we can also combine the clustering with other spatial data sets, such as vegetation height derived from lidar point clouds (e.g., Figure 13) or potentially with other satellite-derived data.

We also compared our clustering algorithm to the standard approach within the literature for analyzing channel networks—normalized channel steepness analysis. We found that the strong lithological variations in the catchment identified by clustering were not detectable when analyzing the distribution of k_{sn} between lithologies (Figure 15). Following on from this, we performed the extraction of channel steepness and concavity metrics (k_s and θ) separately for each cluster and found that there was a significant variation in θ between the weaker shale lithology and more resistant volcanics that is not possible to determine from performing channel steepness analysis prior to clustering. This illustrates how our technique can successfully identify heterogeneity within the landscape, which is not possible with current methods, as well as improving our understanding of controls on river profile morphology.

7. Conclusions

We have presented a new technique for identifying groups of similar river profiles within heterogeneous landscapes. Our method is based on agglomerative hierarchical clustering algorithms commonly used to analyze time series data and allows the classification of river long profiles based on their dissimilarity. With the exponential increase in the global availability of topographic data, particularly at high spatial resolutions, there is a greater need for techniques which allow the efficient analysis of large data sets to extract meaningful geomorphic metrics. A key advantage of a clustering approach is that it allows a significant reduction in data density: we can combine tens to thousands of river profiles into groups with similar morphologies. This potentially allows the extraction of signals from the aggregated statistics of each group which would not be possible if each profile was analyzed in isolation.

This approach can potentially be useful for a variety of geomorphic problems. By analyzing the characteristic profiles of each cluster, we can investigate both the overall differences in channel morphology between clusters as well as patterns of gradient within each cluster. We can use these spatial differences to interpret each group in terms of common lithological, climatic, or tectonic drivers. We have demonstrated through a number of synthetic and real-world examples that clustering can distinguish and spatially map both variations in lithology and landscape transience from migrating incision waves. We have shown that we can use clustering to detect scaling breaks between debris flow-dominated and fluvial-dominated process regimes, as well as improving our ability to extract metrics of channel steepness and concavity. Although we focus here on the use of clustering in tectonic geomorphology, classifying morphologically similar river profiles could also be used to tackle diverse problems such as identifying hillslope-valley transitions; exploring controls on channel initiation; and understanding the transition between bedrock and alluvial rivers.

Acknowledgments

The authors would like to thank Noah Snyder, Patrick Bogaart, and two anonymous reviewers for constructive comments that helped to improve the manuscript. Clubb was supported by a Geo.X fellowship. The code for the extraction of river profiles, performing the clustering analysis, and plotting the data is available from the GFZ Data Services (Clubb et al., 2019), and the development version is freely available through GitHub (<https://github.com/UP-RS-ESP/river-clusters>). We also thank Nina Bingham for providing the lithological data for the Pozo catchment, which can be found in the supporting information. We provide the parameter files for running and analyzing both the real and synthetic landscapes in the supporting information. The point clouds used to create the DEM for the Pozo catchment are available from the 2010 U.S. Geological Survey Channel Islands Lidar Collection (<http://opentopo.sdsc.edu/datasetMetadata?otCollectionID=OT.082012.26911.1>), and the point cloud and raster data for Harrington Creek can be downloaded from OpenTopography (<http://opentopo.sdsc.edu/datasetMetadata?otCollectionID=OT.082012.26911.2>).

References

- Abido, M. A. (2003). Environmental/economic power dispatch using multiobjective evolutionary algorithms. *IEEE Transactions on Power Systems*, 18(4), 1529–1537. <https://doi.org/10.1109/TPWRS.2003.818693>
- Abrahams, A. D. (1984). Channel networks: A geomorphological perspective. *Water Resources Research*, 20(2), 161–188. <https://doi.org/10.1029/WR020i002p0016>
- Aghabozorgi, S., Seyed Shirkarshidi, A., & Ying Wah, T. (2015). Time-series clustering – A decade review. *Information Systems*, 53, 16–38. <https://doi.org/10.1016/j.is.2015.04.007>
- Aiken, S. J., & Briner, G. J. (2013). Analysis of longitudinal profiles along the eastern margin of the Qinghai-Tibetan Plateau. *Journal of Mountain Science*, 10(4), 643–657. <https://doi.org/10.1007/s11629-013-2814-2>
- Anthony, D. M., & Granger, D. E. (2007). An empirical stream power formulation for knickpoint retreat in Appalachian Plateau fluviokarst. *Journal of Hydrology*, 343, 117–126. <https://doi.org/10.1016/j.jhydrol.2007.06.013>
- Bookhagen, B., & Strecker, M. R. (2012). Spatiotemporal trends in erosion rates across a pronounced rainfall gradient: Examples from the southern Central Andes. *Earth and Planetary Science Letters*, 327–328, 97–110. <https://doi.org/10.1016/j.epsl.2012.02.005>
- Braun, J., Simon-Labric, T., Murray, K. E., & Reiners, P. W. (2014). Topographic relief driven by variations in surface rock density. *Nature Geoscience*, 7(7), 534–540. <https://doi.org/10.1038/ngeo2171>
- Braun, J., & Willett, S. D. (2013). A very efficient O(n), implicit and parallel method to solve the stream power equation governing fluvial incision and landscape evolution. *Geomorphology*, 180–181, 170–179. <https://doi.org/10.1016/j.geomorph.2012.10.008>
- Clubb, F. J., Bookhagen, B., & Rheinwald, A. (2019). river-clusters: Clustering river profiles from topographic data, v1.0.GFZ Data Services, <https://doi.org/10.5880/fidgeo.2019.006>

- Clubb, F. J., Mudd, S. M., Attal, M., Milodowski, D. T., & Grieve, S. W. (2016). The relationship between drainage density, erosion rate, and hilltop curvature: Implications for sediment transport processes. *Journal of Geophysical Research: Earth Surface*, 121, 1724–1745. <https://doi.org/10.1002/2015JF003747>
- Clubb, F. J., Mudd, S. M., Milodowski, D. T., Hurst, M. D., & Slater, L. J. (2014). Objective extraction of channel heads from high-resolution topographic data. *Water Resources Research*, 50, 4283–4304. <https://doi.org/10.1002/2013WR015167>
- Collins, D. B. G., & Bras, R. L. (2010). Climatic and ecological controls of equilibrium drainage density, relief, and channel concavity in dry lands. *Water Resources Research*, 46, W04508. <https://doi.org/10.1029/2009WR008615>
- DiBiase, R. A., Whipple, K. X., Heimsath, A. M., & Ouimet, W. B. (2010). Landscape form and millennial erosion rates in the San Gabriel Mountains, CA. *Earth and Planetary Science Letters*, 289(1-2), 134–144. <https://doi.org/10.1016/j.epsl.2009.10.036>
- Dibblee, T. W. (2001). *Geologic map of Western Santa Cruz Island*. Santa Cruz Island: Dibblee Geological Foundation.
- Duvall, A., Kirby, E., & Burbank, D. (2004). Tectonic and lithologic controls on bedrock channel profiles and processes in coastal California. *Journal of Geophysical Research*, 109, F03002. <https://doi.org/10.1029/2003JF000086>
- Eisen, M. B., Spellman, P. T., Brown, P. O., & Botstein, D. (1998). Cluster analysis and display of genome-wide expression patterns. *Proceedings of the National Academy of Sciences*, 95(25), 14,863–14,868.
- Flint, J. J. (1974). Stream gradient as a function of order, magnitude, and discharge. *Water Resources Research*, 10(5), 969–973. <https://doi.org/10.1029/WR010i005p00969>
- Fournier, A., Fussell, D., & Carpenter, L. (1982). Computer rendering of stochastic models. *Communications of the ACM*, 25(6), 371–384. <https://doi.org/10.1145/358523.358533>
- Giachetta, E., & Willett, S. D. (2018). Effects of river capture and sediment flux on the evolution of plateaus: Insights from numerical modeling and river profile analysis in the Upper Blue Nile Catchment. *Journal of Geophysical Research: Earth Surface*, 123, 1187–1217. <https://doi.org/10.1029/2017JF004252>
- Gilbert, G. (1877). *Geology of the Henry Mountains*, Unnumbered Series. Washington, D. C.: Government Printing Office.
- Girvan, M., & Newman, M. E. J. (2002). Community structure in social and biological networks. *Proceedings of the National Academy of Sciences*, 99(12), 7821–7826. <https://doi.org/10.1073/pnas.122653799>
- Gran, K. B., Finnegan, N., Johnson, A. L., Belmont, P., Wittkop, C., & Rittenour, T. (2013). Landscape evolution, valley excavation, and terrace development following abrupt postglacial base-level fall. *Geological Society of America Bulletin*, 125(11–12), 1851–1864. <https://doi.org/10.1130/B30772.1>
- Grieve, S. W., Mudd, S. M., & Hurst, M. D. (2016). How long is a hillslope? *Earth Surface Processes and Landforms*, 41(8), 1039–1054. <https://doi.org/10.1002/esp.3884>
- Grieve, S. W. D., Mudd, S. M., Milodowski, D. T., Clubb, F. J., & Furbish, D. J. (2016). How does grid-resolution modulate the topographic expression of geomorphic processes? *Earth Surface Dynamics*, 4(3), 627–653. <https://doi.org/10.5194/esurf-4-627-2016>
- Harkins, N., Kirby, E., Heimsath, A., Robinson, R., & Reiser, U. (2007). Transient fluvial incision in the headwaters of the Yellow River, northeastern Tibet, China. *Journal of Geophysical Research*, 112, F03S04. <https://doi.org/10.1029/2006JF000570>
- Hergarten, S., Robl, J., & Stüwe, K. (2016). Tectonic geomorphology at small catchment sizes – extensions of the stream-power approach and the χ method. *Earth Surface Dynamics*, 4(1), 1–9. <https://doi.org/10.5194/esurf-4-1-2016>
- Hobley, D. E. J., Sinclair, H. D., & Mudd, S. M. (2012). Reconstruction of a major storm event from its geomorphic signature: The Ladakh floods, 6 August 2010. *Geology*, 40(6), 483–486. <https://doi.org/10.1130/G32935.1>
- Hooshyar, M., Singh, A., & Wang, D. (2017). Hydrologic controls on junction angle of river networks. *Water Resources Research*, 53, 4073–4083. <https://doi.org/10.1002/2016WR020267>
- Horton, R. E. (1945). Erosional development of streams and their drainage basins; hydrophysical approach to quantitative morphology. *Geological Society of America Bulletin*, 56(3), 275–370. [https://doi.org/10.1130/0016-7606\(1945\)56\[275:EDOSAT\]2.0.CO;2](https://doi.org/10.1130/0016-7606(1945)56[275:EDOSAT]2.0.CO;2)
- Howard, A. D. (1971a). Optimal angles of stream junction: Geometric, stability to capture, and minimum power criteria. *Water Resources Research*, 7(4), 863–873. <https://doi.org/10.1029/WR007i004p00863>
- Howard, A. D. (1971b). Simulation of stream networks by headword growth and branching. *Geographical Analysis*, 3(1), 29–50. <https://doi.org/10.1111/j.1538-4632.1971.tb00346.x>
- Hurst, M. D., Mudd, S. M., Walcott, R., Attal, M., & Yoo, K. (2012). Using hilltop curvature to derive the spatial distribution of erosion rates. *Journal of Geophysical Research*, 117, F02017. <https://doi.org/10.1029/2011JF002057>
- Istanbulluoglu, E., & Bras, R. L. (2005). Vegetation-modulated landscape evolution: Effects of vegetation on landscape processes, drainage density, and topography. *Journal of Geophysical Research*, 110, F02012. <https://doi.org/10.1029/2004JF000249>
- Jain, A. K. (2010). Data clustering: 50 years beyond K-means. *Pattern Recognition Letters*, 31(8), 651–666. <https://doi.org/10.1016/j.patrec.2009.09.011>
- Jain, A. K., Murty, M. N., & Flynn, P. J. (1999). Data clustering: A review. *ACM Computing Surveys*, 31(3), 264–323. <https://doi.org/10.1145/331499.331504>
- Khosravipour, A., Skidmore, A. K., Isenburg, M., Wang, T., & Hussin, Y. A. (2014). Generating pit-free canopoy height models from airborne lidar. *Photogrammetric Engineering & Remote Sensing*, 80(9), 863–872. <https://doi.org/10.14358/PERS.80.9.863>
- Kirby, E., & Whipple, K. (2001). Quantifying differential rock-uplift rates via stream profile analysis. *Geology*, 29(5), 415–418. [https://doi.org/10.1130/0091-7613\(2001\)029<0415:QDRURV>2.0.CO;2](https://doi.org/10.1130/0091-7613(2001)029<0415:QDRURV>2.0.CO;2)
- Kirby, E., & Whipple, K. X. (2012). Expression of active tectonics in erosional landscapes. *Journal of Structural Geology*, 44, 54–75. <https://doi.org/10.1016/j.jsg.2012.07.009>
- Kirby, E., Whipple, K. X., Tang, W., & Chen, Z. (2003). Distribution of active rock uplift along the eastern margin of the Tibetan Plateau: Inferences from bedrock channel longitudinal profiles. *Journal of Geophysical Research*, 108(B4), 2217. <https://doi.org/10.1029/2001JB000861>
- Lavé, J., & Avouac, J. P. (2001). Fluvial incision and tectonic uplift across the Himalayas of central Nepal. *Journal of Geophysical Research*, 106(B11), 26,561–26,591. <https://doi.org/10.1029/2001JB000359>
- Lewis, R. S., & Stanford, L. R. (2002). Digital geologic map compilation of the western half of the Nez Perce Pass 30 × 60 minute quadrangle, Idaho. University of Idaho, Moscow, ID, Idaho Geological Survey.
- Liao, T. W. (2005). Clustering of time series data-survey. *Pattern Recognition*, 38(11), 1857–1874. <https://doi.org/10.1016/j.patcog.2005.01.025>
- March, S. T. (1983). Techniques for structuring database records. *ACM Computing Surveys*, 15(1), 45–79. <https://doi.org/10.1145/356904>
- Maschler, F., Geier, F., Bookhagen, B., & Müller, E. (2018). Locality-based graph clustering of spatially embedded time series. In C. Cherifi, H. Cherifi, M. Karsai, & M. Musolesi (Eds.), *Studies in computational intelligence, Complex Networks & Their Applications VI* (Vol. 689, pp. 719–730). Cham, Switzerland: Springer International Publishing.

- Melton, M. A. (1957). An analysis of the relations among elements of climate, surface properties, and geomorphology, 11.
- Milodowski, D. T., Mudd, S. M., & Mitchard, E. T. A. (2015). Topographic roughness as a signature of the emergence of bedrock in eroding landscapes. *Earth Surface Dynamics*, 3(4), 483–499. <https://doi.org/10.5194/esurf-3-483-2015>
- Morisawa, M. E. (1962). Quantitative geomorphology of some watersheds in the Appalachian Plateau. *Geological Society of America Bulletin*, 73(9), 1025–1046. [https://doi.org/10.1130/0016-7606\(1962\)73\[1025:QGOSWI\]2.0.CO;2](https://doi.org/10.1130/0016-7606(1962)73[1025:QGOSWI]2.0.CO;2)
- Mudd, S. M. (2016). Detection of transience in eroding landscapes. *Earth Surface Processes and Landforms*, 42, 24–41. <https://doi.org/10.1002/esp.3923>
- Mudd, S. M., Attal, M., Milodowski, D. T., Grieve, S. W., & Valters, D. A. (2014). A statistical framework to quantify spatial variation in channel gradients using the integral method of channel profile analysis. *Journal of Geophysical Research: Earth Surface*, 119, 138–152. <https://doi.org/10.1002/2013JF002981>
- Mudd, S. M., Clubb, F. J., Gailleton, B., & Hurst, M. D. (2018). How concave are river channels? *Earth Surface Dynamics*, 6(2), 505–523. <https://doi.org/https://doi.org/10.5194/esurf-6-505-2018>
- Muhs, D. R., Simmons, K. R., Schumann, R. R., Groves, L. T., DeVogel, S. B., Minor, S. A., & Laurel, D. (2014). Coastal tectonics on the eastern margin of the Pacific Rim: Late Quaternary sea-level history and uplift rates, Channel Islands National Park, California, USA. *Quaternary Science Reviews*, 105, 209–238. <https://doi.org/10.1016/j.quascirev.2014.09.017>
- Müller, D. (2011). Modern hierarchical, agglomerative clustering algorithms. arXiv:1109.2378 [cs, stat], arXiv: 1109.2378.
- Murtagh, F., & Contreras, P. (2012). Algorithms for hierarchical clustering: An overview. *Wiley Interdisciplinary Reviews: Data Mining and Knowledge Discovery*, 2(1), 86–97. <https://doi.org/10.1002/widm.53>
- Neely, A. B., Bookhagen, B., & Burbank, D. W. (2017). An automated knickzone selection algorithm (KZ-Picker) to analyze transient landscapes: Calibration and validation. *Journal of Geophysical Research: Earth Surface*, 122, 1236–1261. <https://doi.org/10.1002/2017JF004250>
- Nennewitz, M., Thiede, R. C., & Bookhagen, B. (2018). Fault activity, tectonic segmentation, and deformation pattern of the western Himalaya on Ma timescales inferred from landscape morphology. *Lithosphere*, 10(5), 632–640. <https://doi.org/10.1130/L681.1>
- O'Callaghan, J. F., & Mark, D. M. (1984). The extraction of drainage networks from digital elevation data. *Computer Vision, Graphics, and Image Processing*, 28(3), 323–344. [https://doi.org/10.1016/S0734-189X\(84\)80011-0](https://doi.org/10.1016/S0734-189X(84)80011-0)
- Oguchi, T. (1997). Drainage density and relative relief in humid steep mountains with frequent slope failure. *Earth Surface Processes and Landforms*, 22(2), 107–120. [https://doi.org/10.1002/\(SICI\)1096-9837\(199702\)22:2<107::AID-ESP680>3.0.CO;2-U](https://doi.org/10.1002/(SICI)1096-9837(199702)22:2<107::AID-ESP680>3.0.CO;2-U)
- Olen, S. M., Bookhagen, B., & Strecker, M. R. (2016). Role of climate and vegetation density in modulating denudation rates in the Himalaya. *Earth and Planetary Science Letters*, 445, 57–67. <https://doi.org/10.1016/j.epsl.2016.03.047>
- Peacock, D. C. P., & Sanderson, D. J. (1991). Displacements, segment linkage and relay ramps in normal fault zones. *Journal of Structural Geology*, 13(6), 721–733. [https://doi.org/10.1016/0191-8141\(91\)90033-F](https://doi.org/10.1016/0191-8141(91)90033-F)
- Pelletier, J. D. (2013). A robust, two-parameter method for the extraction of drainage networks from high-resolution digital elevation models (DEMs): Evaluation using synthetic and real-world DEMs. *Water Resources Research*, 49, 75–89. <https://doi.org/10.1029/2012WR012452>
- Perron, J. T., & Royden, L. (2013). An integral approach to bedrock river profile analysis. *Earth Surface Processes and Landforms*, 38(6), 570–576. <https://doi.org/10.1002/esp.3302>
- Perroy, R. (2009). Quantifying land degradation and vegetation recovery on southwestern Santa Cruz Island, California ((Unpublished doctoral dissertation)), Santa Barbara, California, UCSB.
- Perroy, R. L., Bookhagen, B., Asner, G. P., & Chadwick, O. A. (2010). Comparison of gully erosion estimates using airborne and ground-based LiDAR on Santa Cruz Island, California. *Geomorphology*, 118(3), 288–300. <https://doi.org/10.1016/j.geomorph.2010.01.009>
- Perroy, R. L., Bookhagen, B., Chadwick, O. A., & Howarth, J. T. (2012). Holocene and Anthropocene landscape change: Arroyo Formation on Santa Cruz Island, California. *Annals of the Association of American Geographers*, 102(6), 1229–1250. <https://doi.org/10.1080/00045608.2012.715054>
- Pinter, N., Lueddecke, S. B., Keller, E. A., & Simmons, K. R. (1998). Late Quaternary slip on the Santa Cruz Island fault, California. *GSA Bulletin*, 110(6), 711–722. [https://doi.org/10.1130/0016-7606\(1998\)110<711:LQSOTS>2.3.CO;2](https://doi.org/10.1130/0016-7606(1998)110<711:LQSOTS>2.3.CO;2)
- Ranjbar, S., Hooshyar, M., Singh, A., & Wang, D. (2018). Quantifying climatic controls on river network branching structure across scales. *Water Resources Research*, 54, 7347–7360. <https://doi.org/10.1029/2018WR022853>
- Rheinwalt, A., Goswami, B., Boers, N., Heitzig, J., Marwan, N., Krishnan, R., & Kurths, J. (2015). Teleconnections in climate networks: A network-of-networks approach to investigate the influence of sea surface temperature variability on monsoon systems. In V. Lakshmanan, E. Gilletland, A. McGovern, & M. Tingley (Eds.), *Machine learning and data mining approaches to climate science* (pp. 23–33). Switzerland: Springer International Publishing.
- Roda-Boluda, D. C., & Whittaker, A. C. (2016). Normal fault evolution and coupled landscape response: Examples from the Southern Apennines, Italy. *Basin Research*, 30(S1), 186–209. <https://doi.org/10.1111/bre.12215>
- Roe, G. H., Montgomery, D. R., & Hallet, B. (2002). Effects of orographic precipitation variations on the concavity of steady-state river profiles. *Geology*, 30(2), 143–146. [https://doi.org/10.1130/0091-7613\(2002\)030<0143:EOOPVO>2.0.CO;2](https://doi.org/10.1130/0091-7613(2002)030<0143:EOOPVO>2.0.CO;2)
- Sangireddy, H., Carothers, R. A., Stark, C. P., & Passalacqua, P. (2016). Controls of climate, topography, vegetation, and lithology on drainage density extracted from high resolution topography data. *Journal of Hydrology*, 537, 271–282. <https://doi.org/10.1016/j.jhydrol.2016.02.051>
- Schwanghart, W., & Scherler, D. (2017). Bumps in river profiles: Uncertainty assessment and smoothing using quantile regression techniques. *Earth Surface Dynamics*, 5(4), 821–839. <https://doi.org/https://doi.org/10.5194/esurf-5-821-2017>
- Seybold, H., Rothman, D. H., & Kirchner, J. W. (2017). Climate's watermark in the geometry of stream networks. *Geophysical Research Letters*, 44, 2272–2280. <https://doi.org/10.1002/2016GL072089>
- Shreve, R. L. (1966). Statistical Law of Stream Numbers. *The Journal of Geology*, 74(1), 17–37. <https://doi.org/10.1086/627137>
- Smith, T., Bookhagen, B., & Rheinwalt, A. (2017). Spatiotemporal patterns of High Mountain Asia's snowmelt season identified with an automated snowmelt detection algorithm, 1987–2016. *The Cryosphere*, 11(5), 2329–2343. <https://doi.org/10.5194/tc-11-2329-2017>
- Snyder, N. P., Whipple, K. X., Tucker, G. E., & Merritts, D. J. (2000). Landscape response to tectonic forcing: Digital elevation model analysis of stream profiles in the Mendocino triple junction region, northern California. *Geological Society of America Bulletin*, 112(8), 1250–1263. [https://doi.org/10.1130/0016-7606\(2000\)112<1250:LRTTFD>2.0.CO;2](https://doi.org/10.1130/0016-7606(2000)112<1250:LRTTFD>2.0.CO;2)
- Stock, J., & Dietrich, W. E. (2003). Valley incision by debris flows: Evidence of a topographic signature. *Water Resources Research*, 39(4), 1089. <https://doi.org/10.1029/2001WR001057>
- Strahler, A. N. (1957). Quantitative analysis of watershed geomorphology. *Transactions, American Geophysical Union*, 38, 913–920. <https://doi.org/10.1029/TR038i006p00913>

- Tarboton, D. G., Bras, R. L., & Rodriguez-Iturbe, I. (1989). Scaling and elevation in river networks. *Water Resources Research*, 25(9), 2037–2051. <https://doi.org/10.1029/WR025i009p02037>
- Ward, J. H. (1963). Hierarchical grouping to optimize an objective function. *Journal of the American Statistical Association*, 58(301), 236–244. <https://doi.org/10.1080/01621459.1963.10500845>
- Whipple, K. X., DiBiase, R. A., Ouimet, W. B., & Forte, A. M. (2017). Preservation or piracy: Diagnosing low-relief, high-elevation surface formation mechanisms. *Geology*, 45(1), 91–94. <https://doi.org/10.1130/G38490.1>
- Whittaker, A. C., Attal, M., Cowie, P. A., Tucker, G. E., & Roberts, G. (2008). Decoding temporal and spatial patterns of fault uplift using transient river long profiles. *Geomorphology*, 100(3-4), 506–526. <https://doi.org/10.1016/j.geomorph.2008.01.018>
- Willett, S. D., McCoy, S. W., Perron, J. T., Goren, L., & Chen, C.-Y. (2014). Dynamic reorganization of river basins. *Science*, 343(6175), 1248765. <https://doi.org/10.1126/science.1248765>
- Wobus, C., Whipple, K. X., Kirby, E., Snyder, N., Johnson, J., Spyropoulos, K., & Sheehan, D. (2006). Tectonics from topography: Procedures, promise, and pitfalls. *Geological Society of America Special Papers*, 398, 55–74. [https://doi.org/10.1130/2006.2398\(04\)](https://doi.org/10.1130/2006.2398(04))
- Wood, R. (2013). Transient hillslope response to an incision wave sweeping up a watershed: A case study from the Salmon River (Masters's Thesis), San Jose State University.